IEEE Access
Multidisciplinary | Rapid Review | Open Access Journal

Received 1 December 2022, accepted 18 December 2022, date of publication 20 December 2022,
date of current version 27 December 2022.

Digital Object Identifier 10.1109/ACCESS.2022.3230988

RESEARCH ARTICLE

Sparse Parameter Estimation and Imaging in mmWave MIMO Radar Systems With Multiple Stationary and Mobile Targets

MEESAM JAFRI, (Student Member, IEEE), SURAJ SRIVASTAVA, (Member, IEEE), SANA ANWER, AND ADITYA K. JAGANNATHAM, (Senior Member, IEEE)
Department of Electrical Engineering, Indian Institute of Technology Kanpur, Kanpur 208016, India

Corresponding author: Meesam Jafri (meesam@iitk.ac.in)

The work of Aditya K. Jagannatham was supported in part by the Qualcomm Innovation Fellowship, and in part by the Arun Kumar Chair Professorship.

ABSTRACT This work conceives novel target detection and parameter estimation schemes in millimeter-wave (mmWave) multiple-input multiple-output (MIMO) radar (mMR) systems for both stationary and mobile targets/radar platform. Initially, the orthogonal matching pursuit (OMP)-based mmR (OmMR) algorithm is proposed for stationary targets to estimate their radar cross-section (RCS) coefficients, angle, range locations together with the number of targets. Next, mMR systems with mobile targets and platform are considered, followed by development of the simultaneous OMP (SOMP)-based mMR (SmMR) algorithm for RCS, angle/range estimation together with their Doppler velocities. The proposed algorithms lead to a significant improvement in performance since they exploit the inherent sparsity of the mMR scattering scene in contrast to the conventional schemes. Two-dimensional (2D) mMR imaging procedures are also presented for both scenarios in the angle, range, and Doppler dimensions. Analytical expressions are derived for the Cramér-Rao bounds (CRBs) for the mean-squared error (MSE) of joint estimation of the RCS coefficients and Doppler velocities. Simulation results demonstrate that proposed schemes perform well even in low signal-to-noise ratio (SNR) scenarios with a few snapshots of the scattering environment and yield improved performance in comparison to existing sparse as well as non-sparse schemes.

INDEX TERMS Millimeter wave (mmWave), MIMO radar, RCS coefficients, Doppler velocity, radar imaging, parameter estimation, sparsity, simultaneous orthogonal matching pursuit.

I. INTRODUCTION

Automotive Radar is a critical and promising technology for autonomous vehicles and driving assistance systems. Automotive radar technology can help avoid traffic congestion and road accidents, enable automatic cruise control (ACC), automatic emergency brakes (AEB) and forward collision warning (FCW) systems, in addition to greatly improving the fuel efficiency [1]. However, it is important to note that the reliability of these functions in autonomous driving systems depends critically on the accuracy of the angle, range and velocity estimates obtained by the radar in a multi-target scenario [2]. Millimeter-wave (mmWave) technology is expected to play a pivotal role in future communication systems due to its ultra-high data rates that can enable various applications such as Vehicle-to-Everything (V2X) [3], body area networks, UAV communication, to name a few [4].

This is well suited also for radar applications, since the mmWave band provides a large bandwidth, which leads to a significantly higher angle and range resolution in radar, thus aiding in the accurate detection of various targets followed by the estimation of their location parameters [1]. The temporal and angular sparsity of the mmWave channel [5] can be efficiently exploited to further improve the accuracy of radar detection and imaging [6]. The small wavelength of signals at mmWave frequencies enables the packing of large antenna arrays on wireless devices of limited sizes. According to the well-known Rayleigh criterion [7], a large antenna array

The associate editor coordinating the review of this manuscript and approving it for publication was Irfan Ahmed.

can significantly strengthen the angular resolution of the radar. Therefore, Multiple-input multiple-output (MIMO) technology, which uses large arrays with multiple transmit and receive antennas for sensing the scattering environment and detection of targets, can lead to a significant improvement in radar performance [8]. This is due to the fact that MIMO technology supports the simultaneous transmission of multiple probing signals followed by the reception of multiple signals reflected by the targets. Therefore, deploying multiple antennas in the radar system enables the transmission of multiple probing signals and also the subsequent reception of multiple reflected copies of the probing signals, which yields increased degrees of freedom obtained via exploiting spatial diversity. This, in turn, leads to enhanced estimation accuracy and better parameter identifiability in comparison to a standard phased-array radar, which transmits phase shifted versions of a single waveform [9], [10], [11], [12]. A brief review of the existing works in this rapidly evolving area of mMR systems is presented next.

A. REVIEW OF EXISTING WORKS

Several techniques have been described in the existing literature on MIMO Radar toward target detection and parameter estimation. Bekkerman et al., in [13] proposed a generalized likelihood ratio test (GLRT) for target detection and maximum likelihood (ML) estimation of target location. However, the implementation of GLRT is computationally complex, especially in a multi-target scenario, as the parameter search space becomes exponentially large. Moreover, the GLRT also requires prior information pertaining to the number of targets, which is infeasible in practice. To overcome this challenge, the authors in [14], proposed two alternative schemes, i.e., the conditional GLRT (cGLRT) and iterative GLRT (iGLRT), which only require searches over one-dimensional spaces instead of the highly complex K-dimensional search required by the GLRT, while achieving a performance close to that of the GLRT for parameter estimation. However, the cGLRT and iGLRT require a large number of snapshots for acceptable performance. Li et al. in [15] proposed a range-angle generalized Likelihood ratio test (RA-GLRT) for target detection with efficient clutter rejection. However, additional degrees of freedom are needed in the range domain to distinguish targets of interest from the clutter. The authors in [16] proposed an ESPRIT-based angle of arrival estimation scheme to generate highly resolvable images of the scattering environment. Their technique employed an intelligent scheme based on the division of time-frequency resources to generate high quality radar snapshots. However, the scheme propounded by them can be computationally expensive since it requires the eigenvalue decomposition of the spatial signal covariance matrix. Yang et al. in [17] described a reduced-dimensional ESPRIT algorithm to lower the dimensionality of the received data prior to estimation of the angles of arrival in a multi-target scenario. Ngai et al. in [18], proposed a suitably refined version of the ESPRIT algorithm, employing the Kalman filter, for the one-dimensional direction finding problem of MIMO radar. The results therein demonstrate that the proposed scheme performs well in a system with a large number of TAs and RAs, and has the ability to resolve all the targets as long as they are fewer in number than the total number of antennas.

Other researchers have presented MIMO radar techniques, such as Capon [19], APES [20] for the detection of multiple targets using data dependent algorithms followed by the estimation of the target location and associated RCS parameters. However, it must be noted that the Capon scheme yields good estimates of target locations, while its RCS coefficient estimates are biased downward. APES on the other hand provides accurate estimates of the RCS coefficients at the expense of a poorer resolution and hence leads to poorer estimation accuracy of the target locations. In [21], the authors proposed a CAPES algorithm, which combines the best features of the Capon and APES algorithms, to refine the estimates of the RCS coefficients and target locations. Zhang et. al in [22] proposed a reduced dimensional Capon (RD-Capon) algorithm which requires only a single dimensional search, thus entailing a substantially lower computational complexity. However, the constraint restricts only the data received for first transmitted signal to be used to estimate the angle of arrival, which results in a performance loss. The authors in the treatise in [23] presented the novel Capon and Approximate Maximum Likelihood (AML) method, termed CAML, to improve the accuracy of RCS estimation. It must be noted that all the above works consider the targets to be located at an identical range, which is not a realistic assumption in practical scenarios. In a rich scattering environment, the multiple targets are often located at distinct angles and ranges [10]. Several schemes to tackle the problem of identification, followed by estimation of the RCS, range and angle parameters were described in works such as [24], [25], [26], and [27] for stationary and mobile targets. Yardibi et. al [24] proposed two non-parametric, viz., iterative adaptive approach (IAA) and its extension, termed IAA-ML, for RCS estimation coupled with target imaging. Roberts et. al, in their treatise in [25], proposed the regularized IAA for mobile targets. However, these schemes incur a significant computational burden owing to the large number of matrix inversions required.

Rawat et. al in [26] developed block least mean squares (BLMS) and fast BLMS (FBLMS) algorithms for the estimation of RCS coefficients and imaging in a MIMO radar system. The fast FBLMS technique was clearly seen to result in improved estimation and imaging performance, together with faster convergence. However, the framework considered in their work, and hence, the techniques described, were restricted to stationary targets and radar platform. In [27], the authors extended the BLMS and FBLMS for scenarios with mobile targets and radar platform. The authors of [28] proposed recursive least squares (RLS)-based adaptive techniques for time-varying RCS coefficient estimation and 2D MIMO radar imaging in the presence of

an unknown number of targets with unknown angles and ranges. In [29], the authors proposed a two-stage parameter estimation technique for automotive MIMO radar. In their scheme, the first stage successfully performs low-complexity three-dimensional peak detection, while the second stage estimates the direction-of-arrival (DOA) via ESPRIT. Furthermore, the authors of [30] proposed a novel cost function for joint estimation of the Doppler frequency and DOA of the targets employing time division multiplexing (TDM) MIMO radar toward resolving the velocity ambiguity for automotive applications. However, the proposed framework therein is only limited to the estimation of velocities lower than a certain maximum velocity and the spectra of signals of targets with velocities higher than the velocity corresponding to the Nyquist rate are still aliased, and hence cannot be accurately estimated. To address this issue, Sohee et al. in [31] proposed a method for velocity estimation while simultaneously resolving the velocity ambiguity in a frequency-modulated continuous wave (FMCW) radar system. The authors of [32] proposed a tensor generalized weighted linear predictor (TGWLP) for a frequency diverse array (FDA) MIMO radar toward parallel estimation of radar parameters.

The significant difference of the previously published works [26], [27], and [28] with respect to the present work is that while the former consider only conventional sub-6 GHz MIMO systems, the current work incorporates mmWave MIMO technology, which is expected to play a crucial role in 5G communication networks due to its ultra-high data rates. This move to 5G mmWave MIMO technology leads to substantial challenges. For instance, note that the conventional techniques, such as least squares (LS)/Linear minimum mean squared error (LMMSE), require the transmission of a large number of probing signals, particularly in high delay spread scenarios. This is because channel estimation using such conventional methods requires an overdetermined system, thus leading to an ill-posed problem when the number of probing signals is lower than the maximum number of channel taps in the finite impulse response (FIR) filter representing the frequency-selective MIMO radar channel. However, all the above papers fail to exploit the inherent sparsity of the scattering environment at mmWave frequencies, arising from the presence of only a few significant non-zero channel taps in the channel response, which can play a crucial role in improving the accuracy of target detection and RCS/location estimation. To overcome this challenge, other approaches such as compressed sensing (CS), the convex-relaxation based least absolute shrinkage and selection operator (Lasso) [33], and the focal underdetermined system solver (FOCUSS) [34], have been proposed for sparse parameter estimation in ill-posed scenarios. However, the performance of Lasso depends critically on a user-defined regularization parameter, while that of FOCUSS suffers from convergence problems. As a further development, Peng et al. [35] proposed sparse Bayesian learning (SBL) based direction of arrival (DOA) estimation in MIMO radar systems with unknown mutual coupling among the antennas. However, the proposed framework is unsuitable for colocated MIMO radar since it involves a large number of computations. The authors of [36] proposed a reduced-complexity SBL for colocated MIMO radar toward DOA estimation. The array data obtained from matched filters is initially subjected to a low complexity transformation, thereby removing redundancies in order to lower the computational complexity. However, the authors therein consider only single dimensional sparsity in the angular domain. Zhao et al. [37] proposed a framework for sparse parameter estimation in bistatic MIMO radars based on l_2 norm minimization employing the residual sum of square (RSS) technique. In their work, the constrained optimization model is initially transformed into an unconstrained optimization model with the aid of Lagrange multipliers. The sparse solution is next obtained by minimizing this unconstrained model. However, the proposed solution requires the inversion of a dictionary matrix, which incurs a high computational complexity. In [38], the authors proposed a two-stage sparse parameter estimation procedure. In the first stage, the estimation problem is transformed into a sparse signal recovery problem, whose solution is determined via a modified version of the sparse learning via iterative minimization (SLIM) technique. In the second stage, a RELAX-based iterative algorithm is employed to refine the estimates obtained via the SLIM algorithm. However, since the proposed method has two stages, and additionally requires the RELAX algorithm to compute the sparse values of the target parameters, it can potentially be resource intensive. Furthermore, the proposed algorithm also suffers from amplitude-related dynamic range issues, which hampers its ability to efficiently exploit the sparsity of the radar parameters. Zhimin et al., in [39], proposed an SBL varaint for phase errors-based DOA estimation, which exploits the target sparsity in the spatial domain. Advantageously, the proposed framework does not require prior knowledge of the phase errors.

Although the works reviewed above focus on sparse parameter estimation in MIMO radar systems, they are based on the conventional fully-digital signal processing architecture at the transmitter and receiver, which demands a separate RF chain for each antenna. This poses significant implementation challenges in the mmWave regime due to the large number of antennas coupled with the high power consumption of the high rate analog-to-digital converters (ADCs) [40]. To overcome this obstacle, novel hybrid analog-digital beamforming architectures were advanced that successfully realized beamforming in mmWave MIMO systems, especially in 5G, which require a much fewer number of RF chains [41], [42], [43]. Thus, motivated by these limitations of the above works in the existing literature, this paper conceives novel techniques for target identification via sparse parameter estimation in mmWave MIMO radar (mMR) systems using hybrid analog-digital beamforming, considering stationary as well as mobile targets and radar platform, which efficiently exploit the sparse nature of

the scattering environment toward improved performance. Table 1 presents a visual comparison of the contributions of the various works discussed above in relation to the current one. The various contributions of our paper are described below in an itemized fashion.

B. CONTRIBUTIONS

This paper focuses on RCS, location estimation and radar imaging for stationary and mobile targets/radar platforms in mMR systems.

1) Initially, a model is developed for mMR systems with stationary targets and radar platform with a specific focus on the sparsity of the mmWave MIMO channel. Subsequently, the orthogonal matching pursuit (OMP)-based mmWave MIMO Radar (OmMR) algorithm is proposed to estimate the RCS coefficients for multiple targets of interest in mMR systems.
2) Next, the proposed model is extended to include mobility of the targets and radar platform with mobility. For this system, the simultaneous orthogonal matching pursuit (SOMP)-based mmWave MIMO Radar (SmMR) technique is developed for joint estimation of the RCS coefficients, angle/range parameters as well as Doppler velocities of the multiple targets using multiple snapshots. Once again, taking advantage of the sparsity leads to a substantial improvement in the estimates. Furthermore, radar imaging algorithms of the scattering environment are presented in the angle and range dimensions as well as the Doppler and range dimensions.
3) Furthermore, closed-form analytical expressions are derived for the Cramér-Rao bounds (CRBs) of the error covariance matrices pertaining to the estimation of the RCS coefficients and Doppler velocities for the stationary and mobile target/radar platform scenarios.
4) Exhaustive simulation results are presented to characterize the RCS coefficient and Doppler velocity estimation performance of the proposed techniques in mMR systems. Results demonstrate that the proposed schemes exploit the inherent sparsity of the clutter environment to yield a significant improvement in comparison to the conventional linear minimum mean squared error (LMMSE) estimator [44] that does not leverage the sparsity, as well as the focal underdetermined system solver (FOCUSS) [34] that is not as efficient in utilizing the sparsity.

The rest of the paper is organized as follows. The mMR system model for stationary targets is developed in section II, followed by the RCS coefficient estimation model. Section III describes the proposed OmMR algorithm for sparse estimation of the RCS coefficient vector, followed by radar imaging. In Section IV, we extend the stationary system model of Section II to incorporate target as well as radar platform mobility. The SmMR algorithm is subsequently developed for joint RCS coefficient and Doppler velocity estimation. Section V derives the closed form analytical expressions for the CRBs pertaining to estimation of the RCS coefficients and Doppler velocities of the multiple targets. Finally, Section VI presents our simulation results to illustrate the performance of the proposed algorithms, followed by the conclusion in Section VII. The intermediate steps in the derivation of the CRBs are presented in Appendix A.

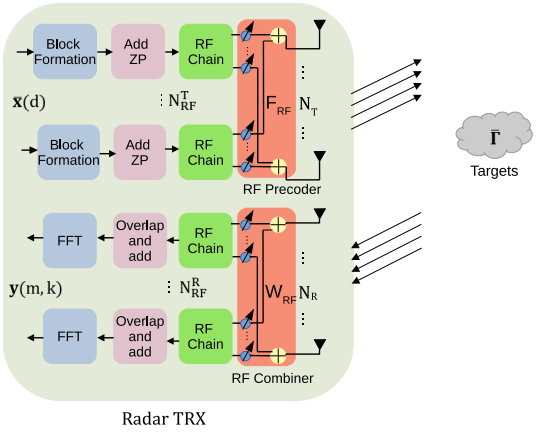

FIGURE 1. Block diagram of mmWave MIMO radar signal processing.

1) NOTATIONS

The following notation is used throughout this paper. Vectors and matrices are denoted by boldfaced lowercase $\mathbf{a}$ and uppercase $\mathbf{A}$, respectively. The quantity $\text{diag}\,(a_1, a_2, \cdots, a_N)$ represents a diagonal matrix with $a_1, a_2, \cdots, a_N$ on the principle diagonal and superscripts $(\cdot)^T$, $(\cdot)^H$, $(\cdot)^*$, $(\cdot)^{-1}$ and $(\cdot)^\dagger$ denote the transpose, Hermitian, conjugation, inverse and pseudoinverse of a matrix or a vector, respectively. The notation $\mathbf{0}_{M\times N}$ denotes matrix of zeros of size $M \times N$. The quantity vec(.) denotes the vector obtained by stacking the columns of a matrix. The quantity $[a]_i$ denotes the ith element of vector $\mathbf{a}$. The quantities $|\cdot|$ and $\angle(\cdot)$ represent the magnitude and phase of a complex quantity. The matrix Kronecker product is denoted by $\otimes$ whereas the l_2-norm and the l_0 norm are represented by $\|\cdot\|_2$ and $\|\cdot\|_0$, respectively. Cardinality of $\mathcal{A}$ is denoted as $|\mathcal{A}|$. The quantity $\mathbf{w} \sim \mathcal{CN}(\boldsymbol{\alpha}, \boldsymbol{\Sigma})$ denotes a circularly symmetric complex Gaussian random vector $\mathbf{w}$ with mean vector $\boldsymbol{\alpha}$ and covariance matrix $\boldsymbol{\Sigma}$. The statistical expectation operator is denoted by $\mathbb{E}\{\cdot\}$.

II. mmWave MIMO RADAR SYSTEM MODEL

Consider a co-located mMR system with N_T transmit antennas (TAs), N_R receive antennas (RAs), N_{RF}^T transmit radio-frequency chains (RFCs) and N_{RF}^R receive RFCs, where $N_{RF}^T \ll N_T$ and $N_{RF}^R \ll N_R$. The hybrid analog-digital beamforming (HAD) architecture leads to a significant reduction in the number of RF chains required for beamforming. The schematic block-diagram of the mMR system is given in Fig. 1. We commence by considering the system model for stationary targets and a stationary radar platform. A comprehensive system model for mobile targets and a mobile radar platform is considered in section IV.

TABLE 1. Comparison of the salient contributions of existing and present works.

Features	[13]	[14]	[15]	[17]	[18]	[22]	[23]	[26]	[28]	[35]	[37]	[38]	Proposed work
mmWave hybrid MIMO radar													✓
Frequency domain model			✓		✓				✓				✓
Sparse estimation				✓						✓	✓	✓	✓
Radar Imaging							✓	✓	✓	✓			✓
Mobile targets				✓	✓	✓	✓		✓	✓	✓	✓	✓
Multiple parameter estimation		✓	✓				✓	✓	✓		✓	✓	✓
Computational effectiveness	✓	✓	✓	✓		✓	✓	✓					✓
Simultaneous-sparsity													✓
CRB	✓	✓						✓	✓		✓	✓	✓
No prior information of targets			✓			✓		✓		✓	✓	✓	✓

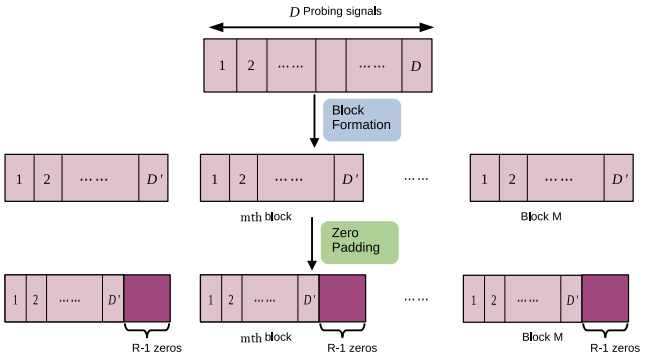

FIGURE 2. mMR frame structure for stationary targets.

The scattering environment can be segmented into Q angular bins and R range bins. Consider L targets to be randomly dispersed within the scattering environment at some unidentified angles and ranges from the radar. Assume all the targets to be in the far field of the radar system, i.e., the distance between the targets and the radar platform is substantially larger than the dimension of the antenna array. The signal echoes are assumed to bounce off all the targets of interest and reach the radar transceiver (TRX). Thus, the signals reaching the targets from the TAs and the signal echos arriving at RAs can be assumed to be parallel. Let $\tilde{\alpha}(q, r)$ denote the RCS coefficient associated with a generic target located at an angle θ_q and range R_r from the radar platform. The transmitted signal is reflected back by a target located at a range R_r, and received at the radar platform after a round trip delay of $\tau_r = 2R_c/c$, where c is the speed of light. The RCS coefficient $\tilde{\alpha}(q, r)$ is set to zero for the (q, r)th bin if no target is present in the bin. We consider a practical scenario where prior information regarding the number of targets and their angle and range bins is unknown to the radar transceiver (TRX). Let $\bar{\mathbf{x}}(d) \in \mathbb{C}^{N_{RF}^T \times 1}$ $0 \leq d \leq D-1$ be the initial probing signal vector at time instant d sent by the radar TRX with covariance matrix $\mathbf{\Sigma}_x = \mathbb{E}\{\bar{\mathbf{x}}(d)\bar{\mathbf{x}}^H(d)\}$. The received echo $\bar{\mathbf{y}}(d) \in \mathbb{C}^{N_{RF}^R \times 1}$ reflected by the L targets and summed over all Q angular bins at time instant d can be written as

$$\bar{\mathbf{y}}(d) = \sum_{q=0}^{Q-1} \mathbf{W}_{\mathrm{RF}}^H \mathbf{a}_R(q)\mathbf{a}_T^H(q)\mathbf{F}_{\mathrm{RF}}\left(\bar{\mathbf{x}}(d) * \tilde{\alpha}(q, d)\right) + \mathbf{W}_{\mathrm{RF}}^H \bar{\mathbf{v}}(d), \tag{1}$$

where $\bar{\mathbf{v}}(d) \in \mathbb{C}^{N_R \times 1}$ represents the Gaussian noise vector at the receiver with covariance matrix $\bar{\sigma}_v^2 I_{N_R}$. The symbol $*$ denotes the linear convolution between the RCS coefficients $\tilde{\alpha}(q, d)$ and probing signal vector $\bar{\mathbf{x}}(d)$. The mMR transmitter consists of the RF transmit precoder (TPC) $\mathbf{F}_{\mathrm{RF}} \in \mathbb{C}^{N_T \times N_{\mathrm{RF}}^T}$. Similarly, the receiver end is equipped with the RF receive combiner (RC) $\mathbf{W}_{\mathrm{RF}} \in \mathbb{C}^{N_R \times N_{RF}^R}$. Note that the RF TPC $\mathbf{F}_{\mathrm{RF}}$ and RF RC $\mathbf{W}_{\mathrm{RF}}$, respectively, comprise digitally controlled phase-shifters with a constant magnitude for each element. Let λ denote the signal wavelength and d_T and d_R denote the spacings between the antenna elements of the transmitter and receiver arrays, respectively. The steering array response vectors $\mathbf{a}_T(q) \in \mathbb{C}^{N_T \times 1}$ and $\mathbf{a}_R(q) \in \mathbb{C}^{N_R \times 1}$, at the transmitter and receiver, respectively, are given by

$$\mathbf{a}_T(q) = \left[1 \;\; e^{-j\frac{2\pi}{\lambda}d_T(1)\sin\theta_q} \;\; \cdots \;\; e^{-j\frac{2\pi}{\lambda}d_T(N_T-1)\sin\theta_q}\right]^T, \tag{2}$$

$$\mathbf{a}_R(q) = \left[1 \;\; e^{-j\frac{2\pi}{\lambda}d_R(1)\sin\theta_q} \;\; \cdots \;\; e^{-j\frac{2\pi}{\lambda}d_R(N_R-1)\sin\theta_q}\right]^T. \tag{3}$$

To simplify the signal processing in a wideband mMR system, this study utilizes a frequency-domain (FD) equalization technique [45]. One can obtain the corresponding FD representation by using the well-known *overlap-and-add* principle. The model to estimate the RCS coefficients is developed next.

A. RCS COEFFICIENTS ESTIMATION MODEL

The probing signal matrix consisting of D snapshots $\mathbf{X}(d) = [\bar{\mathbf{x}}(0), \cdots, \bar{\mathbf{x}}(D-1)] \in \mathbb{C}^{N_{RF}^T \times D}$ is grouped into M sub-blocks, where the mth block, $0 \leq m \leq M-1$, is of length $D' < D$ as shown in Fig. 2. Let $\bar{\mathbf{x}}(m, d') \in \mathbb{C}^{N_{RF}^T \times 1}$ represent the d'th, $0 \leq d' \leq D'-1$, probing vector of the mth block. The "Add ZP" block in Fig. 1 pads all the M blocks with $R-1$ zeros. The new block length of the zero-padded (ZP) probing sequence equals $K = D' + R - 1$ with $\bar{\mathbf{x}}(m, l)_{l=0}^{K-1}$ denoting the probing sequences. The RCS coefficient parameter sequence $\tilde{\alpha}(q, d')$ of length R is padded with $D'-1$ zeros to obtain the ZP sequence $\tilde{\alpha}(q, l)_{l=0}^{K-1}$. One can represent the ZP probing sequence and RCS coefficient

sequence as

$$\{\bar{\mathbf{x}}(m,l)\}_{l=0}^{K-1} = \{\bar{\mathbf{x}}(m,0),\ \bar{\mathbf{x}}(m,1),\ \cdots,\ \bar{\mathbf{x}}(m,D'-1),\ \underbrace{\mathbf{0},\ \cdots,\ \mathbf{0}}_{R-1}\}, \quad (4)$$

$$\{\tilde{\alpha}(q,l)\}_{l=0}^{K-1} = \{\tilde{\alpha}(q,0),\ \tilde{\alpha}(q,1),\ \cdots,\ \tilde{\alpha}(q,R-1),\ \underbrace{0,\ \cdots,\ 0}_{D'-1}\}. \quad (5)$$

The received signal vector after RF combining $\bar{\mathbf{y}}(m,l) \in \mathbb{C}^{N_{RF}^R \times 1}$, $0 \le l \le K-1$ for the mth block, corresponding to the time index l, is given by

$$\bar{\mathbf{y}}(m,l) = \sum_{q=0}^{Q-1} \mathbf{W}_{\mathrm{RF},m}^H \mathbf{a}_R(q)\mathbf{a}_T^H(q)\mathbf{F}_{\mathrm{RF},m}\left(\bar{\mathbf{x}}(m,l) \circledast_K \tilde{\alpha}(q,l)\right) + \mathbf{W}_{\mathrm{RF},m}^H \bar{\mathbf{v}}(m,l), \quad (6)$$

where $\mathbf{F}_{\mathrm{RF},m} \in \mathbb{C}^{N_T \times N_{RF}^T}$ and $\mathbf{W}_{\mathrm{RF},m} \in \mathbb{C}^{N_R \times N_{RF}^R}$ represent the RF TPC and RF RC, for the mth block, respectively, and $\circledast_K$ denotes the K-point circular convolution between the sequences $\bar{\mathbf{x}}(m,l)$ and $\tilde{\alpha}(q,l)$. The mth frequency domain (FD) output block $\{\mathbf{y}[m,k]\}_{k=0}^{K-1} \in \mathbb{C}^{N_{RF}^R \times K}$ is obtained as

$$\{\mathbf{y}[m,k]\}_{k=0}^{K-1} = \mathrm{FFT}\left(\{\bar{\mathbf{y}}(m,l)\}_{l=0}^{K-1}\right) = \{\mathbf{y}[m,0],\ \mathbf{y}[m,1],\ \cdots,\ \mathbf{y}[m,K-1]\}. \quad (7)$$

The received signal vector for the mth block and kth subcarrier can be written as

$$\mathbf{y}[m,k] = \sum_{q=0}^{Q-1} \mathbf{W}_{RF,m}^H \mathbf{a}_R(q)\mathbf{a}_T^H(q)\mathbf{F}_{RF,m}\mathbf{x}[m,k]\alpha[q,k] + \mathbf{W}_{RF,m}^H \mathbf{v}[m,k], \quad (8)$$

where $\mathbf{v}[m,k] \in \mathbb{C}^{N_R \times 1}$ and $\mathbf{x}[m,k] \in \mathbb{C}^{N_{RF}^T \times 1}$ represent the kth FFT-point of the noise vector $\mathbf{v}(m,l)$ and probing signal vector $\bar{\mathbf{x}}(m,l)$, respectively. Also, note that variance of each element of $\mathbf{v}[m,k]$ is $\sigma_v^2 = K\bar{\sigma}_v^2$. The TD probing signal vector for the mth block is given as

$$\bar{\mathbf{x}}(m,l)_{l=0}^{K-1} = \mathbf{x}(m) \times \mathrm{IFFT}(s[m,k])_{k=0}^{K-1}, \quad (9)$$

where $\{s[m,k]\}$ represents a known random sequence of symbols with $s[m,k] \in \{+1,-1\}$. After multiplying both sides of (8) with $s[m,k]$, one can define $\bar{\boldsymbol{\omega}}(m,q) \in \mathbb{C}^{N_{RF}^R \times 1}$ as

$$\bar{\boldsymbol{\omega}}(m,q) = \mathbf{W}_{RF,m}^H \mathbf{a}_R(q)\mathbf{a}_T^H(q)\mathbf{F}_{RF,m}\,\mathbf{x}(m). \quad (10)$$

Next, concatenate $\{\bar{\boldsymbol{\omega}}(m,q)\}_{q=0}^{Q-1}$ for all the angular bins to obtain the common sensing matrix $\bar{\Omega}(m) \in \mathbb{C}^{N_{RF}^R \times Q}$ across all the subcarriers of the mth block as

$$\bar{\Omega}(m) = [\bar{\boldsymbol{\omega}}(m,0)\ \ \bar{\boldsymbol{\omega}}(m,1)\ \ \cdots\ \ \bar{\boldsymbol{\omega}}(m,Q-1)]. \quad (11)$$

The RCS coefficient vector for kth subcarrier is represented as

$$\tilde{\boldsymbol{\gamma}}[k] = [\alpha[0,k]\ \ \alpha[1,k]\ \ \cdots\ \ \alpha[Q-1,k]]^T,$$

where elements of $\tilde{\boldsymbol{\gamma}}[k] \in \mathbb{C}^{Q\times 1}$ denote the kth component of the K-point FFT of the RCS coefficients $\tilde{\alpha}(q,l)$. Thus, (8) can be re-written as

$$\mathbf{y}[m,k] = \bar{\Omega}(m)\tilde{\boldsymbol{\gamma}}[k] + \tilde{\mathbf{v}}[m,k], \quad (12)$$

where $\tilde{\mathbf{v}}[m,k] = \mathbf{W}_{RF,m}^H \mathbf{v}[m,k]$, which follows the Gaussian distribution $\mathcal{CN}\left(\mathbf{0}_{N_{RF}^R\times 1}, \bar{\sigma}_v^2 \Sigma_{N_{RF}^R}\right)$, with $\Sigma_{N_{RF}^R} = K\mathbf{W}_{RF,m}^H\mathbf{W}_{RF,m}$ as its covariance matrix. One can now horizontally concatenate $\mathbf{y}[m,k]$ across all the K sub-carriers, to form the output receive matrix $\mathbf{Y}(m) = [\mathbf{y}[m,0]\ \mathbf{y}[m,1]\ \cdots\ \mathbf{y}[m,K-1]] \in \mathbb{C}^{N_{RF}^R \times K}$. The sparse parameter estimation model for the mMR system can be reformulated as

$$\mathbf{Y}(m) = \bar{\Omega}(m)\boldsymbol{\Gamma} + \mathbf{V}(m), \quad (13)$$

where $\mathbf{V}(m) = \left[\tilde{\mathbf{v}}[m,0]\ \tilde{\mathbf{v}}[m,1]\ \cdots\ \tilde{\mathbf{v}}[m,K-1]\right] \in \mathbb{C}^{N_{RF}^R \times K}$ and $\boldsymbol{\Gamma} = \left[\tilde{\boldsymbol{\gamma}}[0]\ \tilde{\boldsymbol{\gamma}}[1]\ \cdots\ \tilde{\boldsymbol{\gamma}}[K-1]\right] \in \mathbb{C}^{Q\times K}$ denote the concatenated noise matrix and the RCS coefficient matrix in the frequency-domain, respectively.

Utilizing the zero-padding done in the time domain, one can express the frequency-domain RCS coefficient matrix $\boldsymbol{\Gamma}$ as $\boldsymbol{\Gamma} = \left[\bar{\boldsymbol{\Gamma}}\ \mathbf{0}_{Q\times(D'-1)}\right]\mathbf{F}$ where $\mathbf{F} \in \mathbb{C}^{K\times K}$ represents the discrete Fourier transform (DFT) matrix. This can be further simplified as $\boldsymbol{\Gamma} = \left[\bar{\boldsymbol{\Gamma}}\ \mathbf{0}_{Q\times(D'-1)}\right]\left[\mathbf{F}_1^T\mathbf{F}_2^T\right]^T = \bar{\boldsymbol{\Gamma}}\mathbf{F}_1$, where $\bar{\boldsymbol{\Gamma}} \in \mathbb{C}^{Q\times R}$ and $\mathbf{F}_1 \in \mathbb{C}^{R\times K}$ represent the RCS coefficient matrix in the time-domain and DFT matrix corresponding to the non ZP component, respectively. The RCS coefficient matrix $\bar{\boldsymbol{\Gamma}}$ in the time-domain is as follows

$$\bar{\boldsymbol{\Gamma}} = \begin{bmatrix} \tilde{\alpha}(0,0) & \cdots & \tilde{\alpha}(0,R-1) \\ \vdots & & \vdots \\ \tilde{\alpha}(Q-1,0) & \cdots & \tilde{\alpha}(Q-1,R-1) \end{bmatrix}, \quad (14)$$

where $\tilde{\alpha}(q,r)$ represents the RCS coefficient of the target present in the (q,r)th bin corresponding to angle θ_q and range R_r with respect to the radar TRX. The coefficient $\tilde{\alpha}(q,r)$ is either zero or non-zero depending on absence or presence, respectively, of a target in the (q,r)th bin. Substituting $\boldsymbol{\Gamma} = \bar{\boldsymbol{\Gamma}}\mathbf{F}_1$ in (13), the parameter estimation model for the mth block can be written as

$$\mathbf{Y}(m) = \bar{\Omega}(m)\bar{\boldsymbol{\Gamma}}\mathbf{F}_1 + \mathbf{V}(m), \quad (15)$$

Applying the vec$(\cdot)$ operator, i.e., $\mathbf{y}(m) = \mathrm{vec}\,(\mathbf{Y}(m))$ to (15), one can reformulate the above model as

$$\mathbf{y}(m) = \underbrace{(\mathbf{F}_1^T \otimes \bar{\Omega}(m))}_{\boldsymbol{\Omega}(m)}\,\bar{\boldsymbol{\gamma}} + \mathbf{v}(m), \quad (16)$$

where $\boldsymbol{\Omega}(m) \in \mathbb{C}^{N_{RF}^R K \times QR} = (\mathbf{F}_1^T \otimes \bar{\Omega}(m))$, while $\bar{\boldsymbol{\gamma}} \in \mathbb{C}^{QR\times 1} = \mathrm{vec}(\bar{\boldsymbol{\Gamma}})$ and $\mathbf{v}(m) \in \mathbb{C}^{N_{RF}^R K\times 1} = \mathrm{vec}(\mathbf{V}(m))$ represent the vectorized form of the RCS coefficients and noise matrix, respectively. Next, one can stack the received output vectors $\mathbf{y}(m)$ for all the M blocks resulting in the final estimation model

$$\mathbf{y} = \boldsymbol{\Omega}\,\bar{\boldsymbol{\gamma}} + \mathbf{v}, \quad (17)$$

Algorithm 1 OmMR for Sparse RCS Estimation

Input: Sensing matrix $\boldsymbol{\Omega}$, output vector $\mathbf{y}$, dictionary matrices $\mathbf{A}_R(\Phi)$ and $\mathbf{A}_T(\Phi)$, stopping parameter ϵ_t

Initialization: Index set $\mathcal{I} = [\,]$, $\boldsymbol{\Omega}^{\mathcal{I}} = [\,]$, residue vectors $\mathbf{r}_{-1} = \mathbf{0}_{N_{RF}^R KN\times 1}$, $\mathbf{r}_0 = \mathbf{y}$, $\widehat{\bar{\boldsymbol{\gamma}}}_{\text{OmMR}} = \mathbf{0}_{QR\times 1}$, counter $i = 0$

while $\left(\left|\,\|\,\mathbf{r}_{i-1}\,\|_2^2 - \|\,\mathbf{r}_i\,\|_2^2\right| \geq \epsilon_t\right)$ **do**

1) $i \leftarrow i + 1$
2) $j = \underset{k=1,\cdots,QR}{\arg\max} \left|\mathbf{r}_{i-1}^H \boldsymbol{\Omega}(:,k)\right|$
3) $\mathcal{I} = \mathcal{I} \cup j$
4) $\boldsymbol{\Omega}^{\mathcal{I}} = \boldsymbol{\Omega}(:,\mathcal{I})$
5) $\widehat{\bar{\boldsymbol{\gamma}}}_{\text{LS}}^i = \left(\boldsymbol{\Omega}^{\mathcal{I}}\right)^{\dagger}\mathbf{y}$
6) $\mathbf{r}_i = \mathbf{y} - \boldsymbol{\Omega}^{\mathcal{I}}\widehat{\bar{\boldsymbol{\gamma}}}_{\text{LS}}^i$

end while

$\widehat{\bar{\boldsymbol{\gamma}}}_{\text{OmMR}}(\mathcal{I}) = \widehat{\bar{\boldsymbol{\gamma}}}_{\text{LS}}^i$

Output: $\widehat{\bar{\boldsymbol{\Gamma}}}_{\text{OmMR}} = \text{vec}^{-1}\left(\widehat{\bar{\boldsymbol{\gamma}}}_{\text{OmMR}}\right)$

where $\boldsymbol{\Omega} \in \mathbb{C}^{N_{RF}^R KM\times QR}$ and $\mathbf{v} \in \mathbb{C}^{N_{RF}^R KM\times 1}$ are obtained by vertically stacking the sensing matrices $\boldsymbol{\Omega}(m)$ and noise vectors $\mathbf{v}(m)$ for all m. Note that the RCS coefficient vector $\bar{\boldsymbol{\gamma}}$ has a sparse structure, i.e., most of the entries of $\bar{\boldsymbol{\gamma}}$ are close to zero, with only a few of them taking significant non-zero values. One can now observe that (17) represents a well-known sparse signal recovery problem. It is worth noting that the sparsity of the RCS coefficient vector was not utilized in [27]. To address this shortcoming, in this work, we develop the appropriate system model to fully exploit sparsity toward efficient and accurate estimation of the RCS parameters.

III. OmMR-BASED RCS ESTIMATION AND RADAR IMAGING

For the radar cross-section (RCS) coefficient estimation model of (17), one can now formulate the following optimization problem to determine a sparse estimate of the RCS coefficient vector $\bar{\boldsymbol{\gamma}}$ as

$$\begin{aligned} &\min_{\bar{\boldsymbol{\gamma}}} \ \|\bar{\boldsymbol{\gamma}}\|_0 \\ &\text{s.t. } \|\mathbf{y} - \boldsymbol{\Omega}\bar{\boldsymbol{\gamma}}\|_2^2 \leq \epsilon_t, \end{aligned} \tag{18}$$

where $\|\cdot\|_0$ represents the l_0-norm, which equals the number of non-zero elements in the vector [46], and ϵ_t represents a tunable parameter, which can be adjusted to vary the observational error. Note that, the optimization problem in (18) is non-convex [47], which renders it challenging to solve using conventional optimization techniques. Therefore, the OmMR procedure is described next toward sparse estimation.

The key steps of the OmMR technique are described next. These are also summarized in Algorithm 1. In Step-2, the algorithm selects the column of the sensing matrix $\boldsymbol{\Omega}$ that attains the maximum projection along residue $\mathbf{r}_{i-1}$. Step-3 updates the index-set $\mathcal{I}$ by incorporating the index j determined in Step-2. Subsequently, Step-4 builds the submatrix $\boldsymbol{\Omega}^{\mathcal{I}}$ of the sensing matrix $\boldsymbol{\Omega}$ by extracting the columns indexed by the set $\mathcal{I}$. Next, Step-5 obtains the intermediate least squares (LS) solution $\widehat{\bar{\boldsymbol{\gamma}}}_{\text{LS}}^i$ using the submatrix $\boldsymbol{\Omega}^{\mathcal{I}}$. Finally, the associated residue vector $\mathbf{r}_i$ is computed using $\boldsymbol{\Omega}^{\mathcal{I}}$ in Step-6. These steps are iterated until the difference between the successive residuals becomes sufficiently small, i.e., $\left|\,\|\,\mathbf{r}_{i-1}\,\|_2^2 - \|\,\mathbf{r}_i\,\|_2^2\right| < \epsilon_t$, where ϵ_t is a suitable threshold. Finally, the estimate of the RCS coefficient matrix $\widehat{\bar{\boldsymbol{\Gamma}}}_{\text{OmMR}} \in \mathbb{C}^{Q\times R}$ is obtained as $\widehat{\bar{\boldsymbol{\Gamma}}}_{\text{OmMR}} = \text{vec}^{-1}\left(\widehat{\bar{\boldsymbol{\gamma}}}_{\text{OmMR}}\right)$. The central advantages of the proposed OmMR algorithm are that it yields a sparse solution and has a low computational complexity. It is important to note that the choice of the stopping parameter ϵ_t plays a prominent role in determining the convergence of the OmMR algorithm.

The radar image can now be obtained as follows. The element $\widehat{\alpha}_{\text{OmMR}}(q,r)$ of the matrix $\widehat{\bar{\boldsymbol{\Gamma}}}_{\text{OmMR}}$ corresponds to the estimate of the RCS coefficient of the target present in the (q,r)th bin. Plotting the magnitudes of the RCS coefficients across the angle/range bins yields the radar intensity image. One can also estimate the number of targets as the number of non-zero entries of the RCS coefficient matrix. The next section develops the system model for RCS and Doppler velocity estimation for a scenario with mobile targets and radar platform.

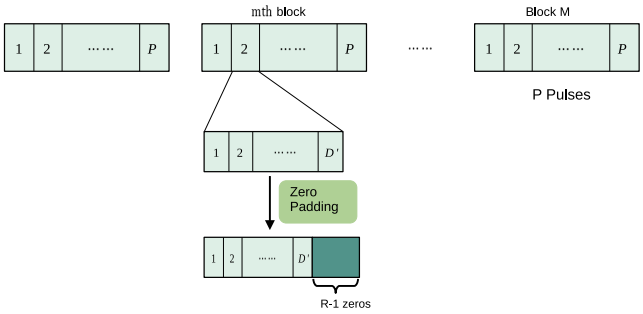

FIGURE 3. mMR frame structure for mobile targets and radar platform.

IV. RCS ESTIMATION AND RADAR IMAGING WITH MOBILITY

The model developed for stationary targets in the previous section can be readily extended for mobile targets incorporating also mobility of the radar platform. The frame-structure for the mobile target and radar platform is given in Fig. 3. The relative Doppler velocity υ_l associated with the lth target can be related to radar platform's linear velocity υ_r, and target's linear velocity $\acute{\upsilon}_l$, as $\upsilon_l = (\upsilon_r - \acute{\upsilon}_l)\cos\theta_l$, where θ_l is the angle between the lth target and radar platform. Consider that the pth pulse, $\bar{\mathbf{x}}(m,p,l)$, $0 \leq p \leq P-1$ in the mth block to be subjected to a Doppler shift of $2\pi\upsilon_l T_m m/\lambda$. The block pulse repetition interval T_m is related to the symbol period T as $T_m = KPT$. Hence, one can recast the system model of (16) for the mobile scenario as

$$\mathbf{y}(m,p) = \boldsymbol{\Omega}(m,p)\underbrace{\text{diag}\left(\mathbf{d}(m)\right)\bar{\boldsymbol{\gamma}}}_{\mathbf{h}(m)} + \mathbf{v}(m,p), \tag{19}$$

where $\mathbf{d}(m) \in \mathbb{C}^{QR\times 1}$ is the Doppler shift vector with the $(q+rQ)$th element defined as $e^{j2\pi \upsilon_{q,r} T_m m/\lambda}$, where $\upsilon_{q,r}$ indicates the relative Doppler velocity of the target present in the (q, r)th bin. The scattering scene vector $\mathbf{h}(m) \in \mathbb{C}^{QR\times 1}$ is defined as the element-wise product of the RCS coefficient vector $\bar{\boldsymbol{\gamma}}$ and Doppler shift vector $\mathbf{d}(m)$ which can be stated as $\mathbf{h}(m) = \text{diag}\,(\mathbf{d}(m))\,\bar{\boldsymbol{\gamma}} = \text{diag}\,(\bar{\boldsymbol{\gamma}})\,\mathbf{d}(m)$. Assume that the scattering scene vector $\mathbf{h}(m)$ is the same for all the P pulses in the mth block. This assumption is justified for an mMR system due to the small symbol period T. Keeping the sensing matrix $\boldsymbol{\Omega}(m, p)$ identical for all the M blocks, the received signal vector $\mathbf{y}(m, p) \in \mathbb{C}^{N_{RF}^R K\times 1}$ in the mth block for the pth pulse is given by

$$\mathbf{y}(m, p) = \boldsymbol{\Omega}(p)\,\mathbf{h}(m) + \mathbf{v}(m, p). \tag{20}$$

Stacking the received signal $\mathbf{y}(m, p)$ across all the $p = 1, \cdots, P$ pulses, the received signal vector in the mth block i.e., $\mathbf{y}(m) \in \mathbb{C}^{N_{RF}^R KP\times 1}$ can be obtained as

$$\underbrace{\begin{bmatrix}\mathbf{y}(m,1)\\ \vdots \\ \mathbf{y}(m,P)\end{bmatrix}}_{\mathbf{y}(m)\in\mathbb{C}^{N_{RF}^R KP\times 1}} = \underbrace{\begin{bmatrix}\Omega(1)\\ \vdots \\ \Omega(P)\end{bmatrix}}_{\Omega\in\mathbb{C}^{N_{RF}^R KP\times QR}} \mathbf{h}(m) + \underbrace{\begin{bmatrix}\mathbf{v}(m,1)\\ \vdots \\ \mathbf{v}(m,P)\end{bmatrix}}_{\mathbf{v}(m)\in\mathbb{C}^{N_{RF}^R KP\times 1}},$$

which can be compactly written as

$$\mathbf{y}(m) = \boldsymbol{\Omega}\,\mathbf{h}(m) + \mathbf{v}(m). \tag{21}$$

The overall received signal matrix $\mathbf{Y}$ can be written as

$$\mathbf{Y} = \boldsymbol{\Omega}\,\mathbf{H} + \mathbf{V}, \tag{22}$$

where $\mathbf{Y} \in \mathbb{C}^{N_{RF}^R KP\times M}$, $\mathbf{H} \in \mathbb{C}^{QR\times M}$ and $\mathbf{V} \in \mathbb{C}^{N_{RF}^R KP\times M}$, which are determined as

$$\begin{aligned}\mathbf{Y} &= [\mathbf{y}(0)\ \ \mathbf{y}(1)\cdots\ \ \mathbf{y}(M-1)],\\ \mathbf{H} &= [\mathbf{h}(0)\ \ \mathbf{h}(1)\ \ \cdots\ \ \mathbf{h}(M-1)],\\ \mathbf{V} &= [\mathbf{v}(0)\ \ \mathbf{v}(1)\ \ \cdots\ \ \mathbf{v}(M-1)],\end{aligned} \tag{23}$$

denote the received signal matrix, scattering scene matrix and noise matrix obtained after horizontal concatenation, respectively. The scattering scene matrix $\mathbf{H}$ has a unique simultaneous sparse structure. Each column of $\mathbf{H}$ has the same sparsity profile which results in several zero rows and a few non-zero rows. The SmMR-based technique can be efficiently employed to obtain an estimate of the scattering scene matrix $\mathbf{H}$, which is discussed next.

A. SmMR-BASED JOINT ESTIMATION OF RCS COEFFICIENTS AND DOPPLER VELOCITIES

The optimization problem for estimation of the scattering scene matrix $\mathbf{H}$ for a mobile radar and target scenario can be stated as follows

$$\begin{aligned}&\arg\min\ \ \|\mathbf{Y} - \boldsymbol{\Omega}\mathbf{H}\|_F\\ &\text{s.t.}\ \ \left\|\text{diag}(\mathbf{H}\mathbf{H}^H)\right\|_0 = QR,\end{aligned} \tag{24}$$

Algorithm 2 SmMR for Sparse Scattering Scene Estimation in Mobile mMR Systems

Input: Dictionary matrix $\boldsymbol{\Omega}$, observation matrix $\mathbf{Y}$ and stopping parameter ϵ_s

Initialization: $\mathcal{I} = [\,]$, residue $\mathbf{R}_0 = \mathbf{Y}$, $\mathbf{R}_{-1} = \mathbf{0}$ $\widehat{\mathbf{H}}_{\text{SmMR}} = \mathbf{0}_{QR\times M}$, counter $k = 0$ $\widetilde{\boldsymbol{\Omega}}^{\mathcal{I}} = [\,]$

while $\left(\|\,\mathbf{R}_{k-1}\,\|_2^2 - \|\,\mathbf{R}_k\,\|_2^2 \geq \epsilon_s\right)$ **do**

1) $k \leftarrow k+1$
2) $\boldsymbol{\Psi} = \boldsymbol{\Omega}^H \mathbf{R}_{k-1}$
3) $i(k) = \arg\max \left[\boldsymbol{\Psi}\boldsymbol{\Psi}^H\right]_{l,l}$
4) $\widetilde{\boldsymbol{\Omega}}_k^{\mathcal{I}} = \left[\widetilde{\boldsymbol{\Omega}}_{k-1}^{\mathcal{I}} | \boldsymbol{\omega}(i(k))\right]$
5) $\widehat{\mathbf{H}}_{\text{SmMR}} = \left((\widetilde{\boldsymbol{\Omega}}_k^{\mathcal{I}})^H \widetilde{\boldsymbol{\Omega}}_k^{\mathcal{I}}\right)^{-1} (\widetilde{\boldsymbol{\Omega}}_k^{\mathcal{I}})^H \mathbf{Y}$
6) $\mathbf{R}_k = \frac{\mathbf{Y} - \widetilde{\boldsymbol{\Omega}}_k^{\mathcal{I}} \widehat{\mathbf{H}}_{\text{SmMR}}}{\|\mathbf{Y} - \widetilde{\boldsymbol{\Omega}}_k^{\mathcal{I}} \widehat{\mathbf{H}}_{\text{SmMR}}\|_F}$

end while

Return: $\widehat{\mathbf{H}}_{\text{SmMR}}$

where $\|\cdot\|_F$ represents the Frobenius-norm. Algorithm 2 describes the proposed SmMR technique for estimation of the matrix $\mathbf{H}$. Step-1 performs a projection of the dictionary column, followed by greedy selection of the columns of $\boldsymbol{\Omega}$ that has the maximum projection along the residue, similar in principle to the OmMR technique. Step-3 updates the submatrix $\widetilde{\boldsymbol{\Omega}}^{\mathcal{I}}$ using indices found in Step-2. Subsequently, the LS estimate of the scattering scene matrix $\widehat{\mathbf{H}}_{\text{SmMR}}$ for the kth iteration is obtained in Step-4. Finally, Step-5 obtains the associated normalized residue $\mathbf{R}_k$. These steps are repeated for $1 \leq k \leq QR$, after the completion of which one obtains the scattering scene matrix estimate $\widehat{\mathbf{H}}_{\text{SmMR}}$. To detect the presence of the target in a particular angle-range bin, an appropriate threshold $\eta_{th} (\ll 1)$ is chosen. The target is considered to be present in the (q, r)th bin if $\frac{1}{M}\sum_{m=0}^{M-1} |[\widehat{\mathbf{h}}_{\text{SmMR}}(m)]_{q+rQ}| \geq \eta_{th}$.

One can now extract the RCS coefficients and Doppler velocities from the estimated scattering scene matrix $\widehat{\mathbf{H}}_{\text{SmMR}}$. Note that the mth column $\hat{\mathbf{h}}_{\text{SmMR}}(m)$ of the matrix $\widehat{\mathbf{H}}_{\text{SmMR}}$, corresponding to the mth block, represents an estimate of the scattering scene vector $\mathbf{h}(m) = \text{diag}\,(\bar{\boldsymbol{\gamma}})\,\mathbf{d}(m)$. The relation between the RCS coefficient vector $\bar{\boldsymbol{\gamma}}$ and columns of scattering scene matrix $\mathbf{H}$ can be expressed as

$$\begin{aligned}&\frac{1}{M-1}\sum_{m=0}^{M-2} (\text{diag}\,(\mathbf{h}(m+1)))^{-m}\,(\text{diag}\,(\mathbf{h}(m)))^{m+1}\\ &= \frac{1}{M-1}\sum_{m=0}^{M-2} (\text{diag}\,(\bar{\boldsymbol{\gamma}}))^{-m}\,(\text{diag}\,(\mathbf{d}(m+1)))^{-m}\\ &\quad\times (\text{diag}\,(\mathbf{d}(m)))^{m+1}\,(\text{diag}\,(\bar{\boldsymbol{\gamma}}))^{m+1} = \text{diag}\,(\bar{\boldsymbol{\gamma}}),\end{aligned}$$

where the last equality stems from the relation

$$(\text{diag}(\mathbf{d}(m+1)))^{-m}(\text{diag}(\mathbf{d}(m)))^{m+1} = \mathbf{I}_{QR}.$$

Thus, one can relate the estimate of the RCS coefficient vector $\widehat{\bar{\boldsymbol{\gamma}}}_{\text{SmMR}}$ to the columns of estimated scattering scene matrix

$\widehat{\mathbf{H}}_{\text{SmMR}}$ as

$$\text{diag}\left(\widehat{\bar{\boldsymbol{\gamma}}}_{\text{SmMR}}\right) = \frac{1}{M-1}\sum_{m=0}^{M-2}\left(\left(\text{diag}\left(\widehat{\bar{\mathbf{h}}}_{\text{SmMR}}(m+1)\right)\right)^{-m} \times \left(\text{diag}\left(\widehat{\bar{\mathbf{h}}}_{\text{SmMR}}(m)\right)\right)^{m+1}\right). \quad (25)$$

Toward estimation of the Doppler velocity υ_l of lth target from the scattering scene matrix, consider the ratio

$$\frac{\left[\bar{\mathbf{h}}(m+1)\right]_l}{\left[\bar{\mathbf{h}}(m)\right]_l} = \frac{[\,\bar{\boldsymbol{\gamma}}\,]_l\, e^{j2\pi\upsilon_l T_m(m+1)/\lambda}}{[\,\bar{\boldsymbol{\gamma}}\,]_l\, e^{j2\pi\upsilon_l T_m m/\lambda}} = e^{j2\pi\upsilon_l T_m/\lambda}. \quad (26)$$

Thus, one can estimate the Doppler velocity υ_l, $0 \le l \le \tilde{L}-1$ as

$$\widehat{\upsilon}_l = \frac{\lambda}{2\pi T_m}\frac{1}{M-1}\sum_{m=0}^{M-2}\angle\left(\frac{\left[\widehat{\bar{\mathbf{h}}}_{\text{SmMR}}(m+1)\right]_{\tilde{q}_l+\tilde{r}_l Q}}{\left[\widehat{\bar{\mathbf{h}}}_{\text{SmMR}}(m)\right]_{\tilde{q}_l+\tilde{r}_l Q}}\right), \quad (27)$$

where $(\tilde{q}_l, \tilde{r}_l)$ denotes the estimated angle and range index pair of the lth target and $\widehat{\mathbf{L}} = |\tilde{\mathcal{I}}|$ is the total number of estimated targets. Note that the estimates of the RCS coefficients and the Doppler velocities are non-linear functions of $\widehat{\mathbf{H}}_{\text{SmMR}}$. Therefore, minor errors in locations of the targets can result in large mean squared errors (MSEs) corresponding to estimation of the RCS coefficients and the Doppler velocities. However, the SmMR technique can overcome these issues efficiently due to its superior ability for sparse recovery.

The next section derives the Cramér-Rao bounds pertaining to the MSEs of RCS and target Doppler velocity estimation in mMR systems.

V. Cramér-RAO BOUNDS

The CRBs are computed in this section for estimation of the RCS coefficient vector $\bar{\boldsymbol{\gamma}}$ and Doppler velocity vector $\boldsymbol{\upsilon} = [\upsilon_1, \cdots, \upsilon_L]^T$, for mMR systems with and without mobility, as derived in equations (16) and (21). Let the effective RCS coefficient vector be defined as $\bar{\boldsymbol{\gamma}}_{\text{ef}} = [\bar{\boldsymbol{\gamma}}_{\mathcal{R}}^T, \bar{\boldsymbol{\gamma}}_{\mathcal{I}}^T]^T \in \mathbb{R}^{2QR\times 1}$, where the real and imaginary components of the RCS coefficient vector are given by $\bar{\boldsymbol{\gamma}}_{\mathcal{R}}$ and $\bar{\boldsymbol{\gamma}}_{\mathcal{I}}$, respectively. The expression to obtain the Fisher information matrix from the log-likelihood function $\mathcal{L}(\mathbf{y};\Theta)$ is given as

$$\mathcal{F}(\mathbf{w},\mathbf{x}) = -\mathbb{E}\left\{\frac{\partial}{\partial \mathbf{w}}\left(\frac{\partial \mathcal{L}(\mathbf{y};\Theta)}{\partial \mathbf{x}^T}\right)\right\}, \quad (28)$$

where $\Theta = [\bar{\boldsymbol{\gamma}}_{\text{ef}}^T, \boldsymbol{\upsilon}^T]^T \in \mathbb{R}^{2QR+L\times 1}$ is the vector of unknown parameters obtained via concatenating $\bar{\boldsymbol{\gamma}}_{\text{ef}}$ and $\boldsymbol{\upsilon}$. Thus, the derived CRBs are applicable for the scenarios without and with mobility, as is appropriate for the particular system. The CRB for joint estimation of the RCS coefficients in $\bar{\boldsymbol{\gamma}}$ and Doppler velocities in $\boldsymbol{\upsilon}$ is given as

$$\text{CRB}(\Theta) = \begin{bmatrix} \mathcal{F}\left(\bar{\boldsymbol{\gamma}}_{\text{ef}}, \bar{\boldsymbol{\gamma}}_{\text{ef}}\right) & \mathcal{F}\left(\bar{\boldsymbol{\gamma}}_{\text{ef}}, \boldsymbol{\upsilon}\right) \\ \mathcal{F}\left(\boldsymbol{\upsilon}, \bar{\boldsymbol{\gamma}}_{\text{ef}}\right) & \mathcal{F}\left(\boldsymbol{\upsilon}, \boldsymbol{\upsilon}\right) \end{bmatrix}^{-1}. \quad (29)$$

The following Lemma derives the equations for the component Fisher information matrices.

Lemma 1: The CR bounds for the RCS coefficient vector $\bar{\boldsymbol{\gamma}}$ and target Doppler velocity vector $\boldsymbol{\upsilon}$ for a system with mobility can be expressed as

$$\text{CRB}\left(\bar{\boldsymbol{\gamma}}_{\text{ef}}\right) = \left[\mathcal{F}\left(\bar{\boldsymbol{\gamma}}_{\text{ef}}, \bar{\boldsymbol{\gamma}}_{\text{ef}}\right) - \mathcal{F}\left(\bar{\boldsymbol{\gamma}}_{\text{ef}}, \boldsymbol{\upsilon}\right)\mathcal{F}^{-1}\left(\boldsymbol{\upsilon}, \boldsymbol{\upsilon}\right)\mathcal{F}\left(\boldsymbol{\upsilon}, \bar{\boldsymbol{\gamma}}_{\text{ef}}\right)\right]^{-1}, \quad (30)$$

$$\text{CRB}\left(\boldsymbol{\upsilon}\right) = \left[\mathcal{F}\left(\boldsymbol{\upsilon}, \boldsymbol{\upsilon}\right) - \mathcal{F}\left(\boldsymbol{\upsilon}, \bar{\boldsymbol{\gamma}}_{\text{ef}}\right)\mathcal{F}^{-1}\left(\bar{\boldsymbol{\gamma}}_{\text{ef}}, \bar{\boldsymbol{\gamma}}_{\text{ef}}\right)\mathcal{F}\left(\bar{\boldsymbol{\gamma}}_{\text{ef}}, \boldsymbol{\upsilon}\right)\right]^{-1}, \quad (31)$$

where the matrix $\mathcal{F}(\bar{\boldsymbol{\gamma}}_{\text{ef}}, \bar{\boldsymbol{\gamma}}_{\text{ef}}) \in \mathbb{R}^{2QR\times 2QR}$ can be derived as

$$\mathcal{F}\left(\bar{\boldsymbol{\gamma}}_{\text{ef}}, \bar{\boldsymbol{\gamma}}_{\text{ef}}\right) = 2\left(\mathbf{I}_2 \otimes \sum_{m=0}^{M-1}\sum_{p=0}^{P-1}\text{diag}(\mathbf{d}(m))\,\boldsymbol{\Sigma}_{\text{c}}\,\text{diag}(\mathbf{d}(m))\right). \quad (32)$$

Further, the components of the Fisher information matrices $\mathcal{F}(\bar{\boldsymbol{\gamma}}_{\text{ef}}, \boldsymbol{\upsilon}) \in \mathbb{R}^{2QR\times L}$ and $\mathcal{F}(\boldsymbol{\upsilon}, \bar{\boldsymbol{\gamma}}_{\text{ef}}) \in \mathbb{R}^{L\times 2QR}$ are given as

$$\mathcal{F}\left(\bar{\boldsymbol{\gamma}}_{\mathcal{R}}, \upsilon_l\right) = 2\sum_{m=0}^{M-1}\sum_{p=0}^{P-1}\left(\text{diag}(\mathbf{d}(m))\,\boldsymbol{\Sigma}_{\text{c}}\,\text{diag}(\dot{\mathbf{d}}_l(m))\bar{\boldsymbol{\gamma}}\right)_{\mathcal{R}},$$
$$\mathcal{F}\left(\bar{\boldsymbol{\gamma}}_{\mathcal{I}}, \upsilon_l\right) = 2\sum_{m=0}^{M-1}\sum_{p=0}^{P-1}\left(\text{diag}(\mathbf{d}(m))\,\boldsymbol{\Sigma}_{\text{c}}\,\text{diag}(\dot{\mathbf{d}}_l(m))\bar{\boldsymbol{\gamma}}\right)_{\mathcal{I}}, \quad (33)$$

where the vector $\dot{\mathbf{d}}_l(m) = \frac{\partial \mathbf{d}(m)}{\partial u_l} \in \mathbb{C}^{QR\times 1}$ is given as

$$\dot{\mathbf{d}}_l(m) = \left[0, \cdots, j\tfrac{2\pi}{\lambda}mT_m\,[\mathbf{d}(m)]_{q_l+r_lQ}, \cdots, 0\right]^T, \quad (34)$$

and the non-zero entry in the vector $\dot{\mathbf{d}}_l(m)$ is at the location $q_l + r_l Q$ for the lth target corresponding to the angle-range bin (q_l, r_l). Note that $\mathcal{F}(\upsilon_l, \bar{\boldsymbol{\gamma}}_{\mathcal{R}}) = (\mathcal{F}(\bar{\boldsymbol{\gamma}}_{\mathcal{R}}, \upsilon_l))^T$ and $\mathcal{F}(\upsilon_l, \bar{\boldsymbol{\gamma}}_{\mathcal{I}}) = (\mathcal{F}\bar{\boldsymbol{\gamma}}_{\mathcal{I}}, \upsilon_l))^T$. The Fisher Information matrix $\mathcal{F}(\upsilon, \upsilon) \in \mathbb{R}^{L\times L}$ has elements $\mathcal{F}(\upsilon_l, \upsilon_{l'})$, $1 \le l, l' \le L$, which can be written as

$$\mathcal{F}\left(\upsilon_l, \upsilon_{l'}\right) = 2\bar{\boldsymbol{\gamma}}^H\sum_{m=0}^{M-1}\sum_{p=0}^{P-1}\text{diag}(\dot{\mathbf{d}}_l^*(m))\,\boldsymbol{\Sigma}_{\text{c}}\,\text{diag}(\dot{\mathbf{d}}_{l'}(m))\bar{\boldsymbol{\gamma}}. \quad (35)$$

Proof: The log likelihood $\mathcal{L}(\mathbf{y};\Theta)$ of the received output vector $\mathbf{y} = \left[\mathbf{y}(0)^T, \mathbf{y}(1)^T, \cdots, \mathbf{y}(M-1)^T\right]^T \in \mathbb{C}^{N_{RF}^R KPM\times 1}$ is given as

$$\mathcal{L}(\mathbf{y};\Theta) = -\kappa - \sum_{m=0}^{M-1}\sum_{p=0}^{P-1}\|\mathbf{y}_{\mathcal{R}}(m,p) - \boldsymbol{\Omega}_{\mathcal{R}}(p)\mathbf{h}_{\mathcal{R}}(m) + \boldsymbol{\Omega}_{\mathcal{I}}(p)\mathbf{h}_{\mathcal{I}}(m)\|^2 - \sum_{m=0}^{M-1}\sum_{p=0}^{P-1}\|\mathbf{y}_{\mathcal{I}}(m,p) - \boldsymbol{\Omega}_{\mathcal{I}}(p)\mathbf{h}_{\mathcal{R}}(m) - \boldsymbol{\Omega}_{\mathcal{R}}(p)\mathbf{h}_{\mathcal{I}}(m)\|^2, \quad (36)$$

where the constant $\kappa = \frac{MPKN_{RF}^{R}}{2} \ln \pi$. The quantities $\frac{\partial \mathcal{L}(\mathbf{y};\Theta)}{\partial \bar{\boldsymbol{\gamma}}_{\mathcal{R}}}$, $\frac{\partial \mathcal{L}(\mathbf{y};\Theta)}{\partial \bar{\boldsymbol{\gamma}}_{\mathcal{I}}}$, $\frac{\partial \mathcal{L}(\mathbf{y};\Theta)}{\partial \upsilon_l}$ can be determined as shown in (37), (38) and (39), as shown at the bottom of the page, respectively.

Other pertinent terms can be obtained as follows

$$\begin{aligned}
&\frac{\partial}{\partial \bar{\boldsymbol{\gamma}}_{\mathcal{R}}}\left(\frac{\partial \mathcal{L}(\mathbf{y};\Theta)}{\partial \bar{\boldsymbol{\gamma}}_{\mathcal{R}}^{T}}\right) \\
&\quad = \frac{\partial}{\partial \bar{\boldsymbol{\gamma}}_{\mathcal{I}}}\left(\frac{\partial \mathcal{L}(\mathbf{y};\Theta)}{\partial \bar{\boldsymbol{\gamma}}_{\mathcal{I}}^{T}}\right) \\
&\quad = -2\sum_{m=0}^{M-1}\sum_{p=0}^{P-1} \operatorname{diag}\left(\mathbf{d}(m)\right) \boldsymbol{\Omega}^{T}(p)\boldsymbol{\Omega}(p)\operatorname{diag}\left(\mathbf{d}(m)\right),
\end{aligned} \tag{41}$$

$$\begin{aligned}
&\frac{\partial}{\partial \bar{\boldsymbol{\gamma}}_{\mathcal{R}}}\left(\frac{\partial \mathcal{L}(\mathbf{y};\Theta)}{\partial \bar{\boldsymbol{\gamma}}_{\mathcal{I}}^{T}}\right) \\
&\quad = \frac{\partial}{\partial \bar{\boldsymbol{\gamma}}_{\mathcal{I}}}\left(\frac{\partial \mathcal{L}(\mathbf{y};\Theta)}{\partial \bar{\boldsymbol{\gamma}}_{\mathcal{R}}^{T}}\right) = \mathbf{0}_{QR,QR}.
\end{aligned} \tag{42}$$

$$\begin{aligned}
&\frac{\partial}{\partial \bar{\boldsymbol{\gamma}}_{\mathcal{R}}}\left(\frac{\partial \mathcal{L}(\mathbf{y};\Theta)}{\partial \upsilon_l}\right) \\
&\quad = \left(\frac{\partial}{\partial \upsilon_l}\left(\frac{\partial \mathcal{L}(\mathbf{y};\Theta)}{\partial \bar{\boldsymbol{\gamma}}_{\mathcal{R}}^{T}}\right)\right)^{T} \\
&\quad = -2\sum_{m=0}^{M-1}\sum_{p=0}^{P-1}\Big(\Big(-\operatorname{diag}\left(\dot{\mathbf{d}}_l(m)\right)\boldsymbol{\Omega}^{T}(p)\mathbf{v}(m,p)\Big)_{\mathcal{R}} \\
&\qquad +\Big(\operatorname{diag}\left(\mathbf{d}(m)\right)\boldsymbol{\Omega}^{T}(p)\boldsymbol{\Omega}(p)\operatorname{diag}\left(\dot{\mathbf{d}}_l(m)\right)\bar{\boldsymbol{\gamma}}\Big)_{\mathcal{R}}\Big),
\end{aligned} \tag{43}$$

$$\begin{aligned}
&\frac{\partial}{\partial \bar{\boldsymbol{\gamma}}_{\mathcal{I}}}\left(\frac{\partial \mathcal{L}(\mathbf{y};\Theta)}{\partial u_l}\right) \\
&\quad = \left(\frac{\partial}{\partial \upsilon_l}\left(\frac{\partial \mathcal{L}(\mathbf{y};\Theta)}{\partial \bar{\boldsymbol{\gamma}}_{\mathcal{I}}^{T}}\right)\right)^{T} \\
&\quad = -2\sum_{m=0}^{M-1}\sum_{p=0}^{P-1}\Big(\Big(-\operatorname{diag}\left(\dot{\mathbf{d}}_l(m)\right)\boldsymbol{\Omega}^{T}(p)\mathbf{v}(m,p)\Big)_{\mathcal{I}} \\
&\qquad +\Big(\operatorname{diag}\left(\mathbf{d}(m)\right)\boldsymbol{\Omega}^{T}(p)\boldsymbol{\Omega}(p)\operatorname{diag}\left(\dot{\mathbf{d}}_l(m)\right)\bar{\boldsymbol{\gamma}}\Big)_{\mathcal{I}}\Big).
\end{aligned} \tag{44}$$

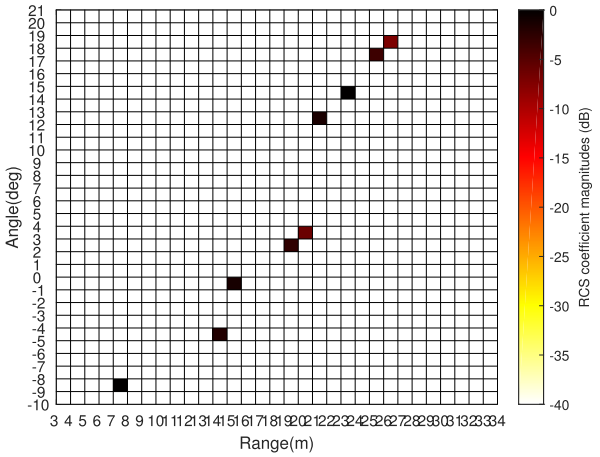

FIGURE 4. Radar image showing the true target locations, i.e., angle and range bins for a stationary scenario.

The detailed procedure to derive these expressions is given in Appendix A. Lastly, the second-order derivative of $\mathcal{L}(\mathbf{y};\Theta)$ with respect to the target Doppler velocity υ_l is given in (40), as shown at the bottom of the page, where $\ddot{\mathbf{d}}_l(m) \in \mathbb{C}^{QR\times 1}$ is given as

$$\begin{aligned}
\ddot{\mathbf{d}}_l(m) &= \frac{\partial^2 \mathbf{d}(m)}{\partial^2 \upsilon_l} \\
&= [0,\cdots,(j\frac{2\pi}{\lambda}mT_m)^2[\mathbf{d}(m)]_{q_l+r_lQ},\cdots,0]^{T}.
\end{aligned} \tag{45}$$

$$\frac{\partial \mathcal{L}(\mathbf{y};\Theta)}{\partial \bar{\boldsymbol{\gamma}}_{\mathcal{R}}} = -2\sum_{m=0}^{M-1}\sum_{p=0}^{P-1}\Big(\Big(\operatorname{diag}\left(\mathbf{d}(m)\right)\boldsymbol{\Omega}^{T}(p)\boldsymbol{\Omega}(p)\operatorname{diag}\left(\mathbf{d}(m)\right)\bar{\boldsymbol{\gamma}}\Big)_{\mathcal{R}} - \Big(\operatorname{diag}\left(\mathbf{d}(m)\right)\boldsymbol{\Omega}^{T}(p)\mathbf{y}(m,p)\Big)_{\mathcal{R}}\Big), \tag{37}$$

$$\frac{\partial \mathcal{L}(\mathbf{y};\Theta)}{\partial \bar{\boldsymbol{\gamma}}_{\mathcal{I}}} = -2\sum_{m=0}^{M-1}\sum_{p=0}^{P-1}\Big(\Big(\operatorname{diag}\left(\mathbf{d}(m)\right)\boldsymbol{\Omega}^{T}(p)\boldsymbol{\Omega}(p)\operatorname{diag}\left(\mathbf{d}(m)\right)\bar{\boldsymbol{\gamma}}\Big)_{\mathcal{I}} - \Big(\operatorname{diag}\left(\mathbf{d}(m)\right)\boldsymbol{\Omega}^{T}(p)\mathbf{y}(m,p)\Big)_{\mathcal{I}}\Big), \tag{38}$$

$$\begin{aligned}
\frac{\partial \mathcal{L}(\mathbf{y};\Theta)}{\partial \upsilon_l} = -\sum_{m=0}^{M-1}\sum_{p=0}^{P-1}\Big(&\mathbf{d}^{H}(m)\operatorname{diag}\left(\bar{\boldsymbol{\gamma}}^{*}\right)\boldsymbol{\Omega}^{H}(p)\boldsymbol{\Omega}(p)\operatorname{diag}\left(\bar{\boldsymbol{\gamma}}\right)\dot{\mathbf{d}}_l(m) - 2\mathbf{y}^{H}(m,p)\boldsymbol{\Omega}(p)\operatorname{diag}\left(\bar{\boldsymbol{\gamma}}\right)\dot{\mathbf{d}}_l(m) \\
&+\dot{\mathbf{d}}_l^{H}(m)\operatorname{diag}\left(\bar{\boldsymbol{\gamma}}^{*}\right)\boldsymbol{\Omega}^{H}(p)\boldsymbol{\Omega}(p)\operatorname{diag}\left(\bar{\boldsymbol{\gamma}}\right)\mathbf{d}(m)\Big),
\end{aligned} \tag{39}$$

$$\begin{aligned}
\frac{\partial}{\partial \upsilon_{l'}}\left(\frac{\partial \mathcal{L}(\mathbf{y};\Theta)}{\partial \upsilon_l}\right) &= -2\sum_{m=0}^{M-1}\sum_{p=0}^{P-1}\dot{\mathbf{d}}_l^{H}(m)\operatorname{diag}\left(\bar{\boldsymbol{\gamma}}^{*}\right)\boldsymbol{\Omega}^{H}(p)\boldsymbol{\Omega}(p)\operatorname{diag}\left(\bar{\boldsymbol{\gamma}}\right)\dot{\mathbf{d}}_{l'}(m), \text{ for } l \neq l', \\
&= -2\sum_{m=0}^{M-1}\sum_{p=0}^{P-1}\Big(\dot{\mathbf{d}}_l^{H}(m)\operatorname{diag}\left(\bar{\boldsymbol{\gamma}}^{*}\right)\boldsymbol{\Omega}^{H}(p)\boldsymbol{\Omega}(p)\operatorname{diag}\left(\bar{\boldsymbol{\gamma}}\right)\dot{\mathbf{d}}_l(m) - \mathbf{v}^{H}(m,p)\boldsymbol{\Omega}(p)\operatorname{diag}\left(\bar{\boldsymbol{\gamma}}\right)\ddot{\mathbf{d}}_l(m)\Big), \text{ for } l = l'.
\end{aligned} \tag{40}$$

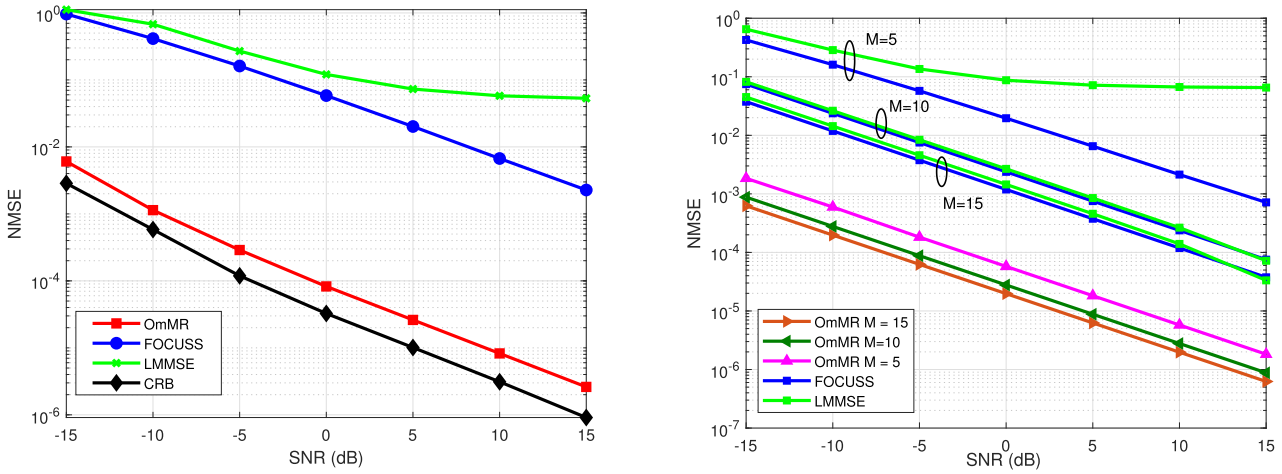

FIGURE 5. Stationary scenario: (a) normalized mean squared error vs. SNR for the proposed OmMR, FOCUSS and LMMSE techniques. (b) Impact of number of snapshots M on the estimation of RCS coefficients using the proposed OmMR, FOCUSS and LMMSE algorithms.

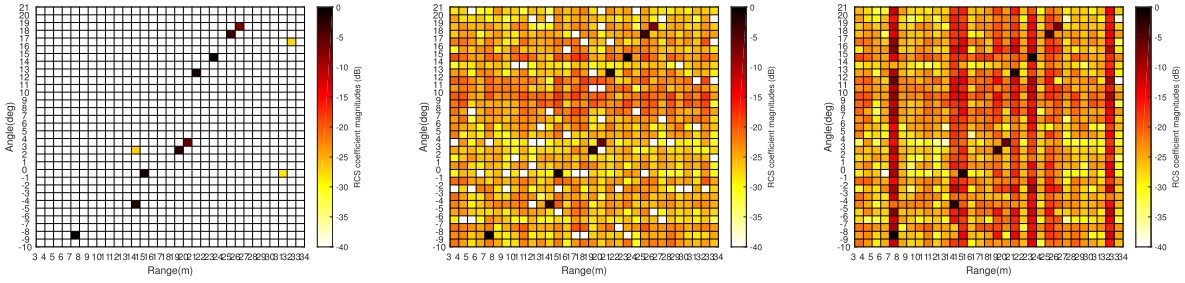

FIGURE 6. Stationary scenario: reconstructed radar images obtained using (a) proposed OmMR, (b) FOCUSS, (c) LMMSE techniques at SNR = −10 dB.

Substituting the various quantities derived above, one can readily obtain the Fisher Information matrices which in turn yield the CRBs in (30), (31). For the case of a stationary mMR system, the unknown parameter vector $\Theta = \bar{\boldsymbol{\gamma}}_{\text{eff}} \in \mathbb{R}^{2QR\times 1}$. The CRB for the estimation of the RCS coefficient vector for this scenario is given as

$$\text{CRB}(\Theta) = \frac{1}{2M}(\mathbf{I}_2 \otimes \boldsymbol{\Sigma}_{\text{c}}^{-1}). \tag{46}$$

VI. SIMULATION RESULTS

This section presents the simulation results to illustrate the performance of the proposed techniques for RCS and Doppler velocity estimation for stationary as well as mobile targets and radar platforms. Consider an mMR TRX with $N_T = 8$ transmit antennas, $N_R = 16$ receive antennas, $N_{RF}^T = 4$ transmit RF chains and $N_{RF}^R = 6$ receive RF chains. The inter-element spacings between the transmit and receive antenna arrays are set to be $d_T = 0.7\lambda$ and $d_R = 0.9\lambda$, respectively, where $\lambda = 0.0107$m for the 28 GHz radar frequency. The number of targets L is set equal to 10, and the scattering environment is divided into $Q = 32$ angular bins and $R = 32$ range bins. The widths of the angular and range bins are $\Delta Q = 1°$ and $\Delta R = 1$ m, respectively. It is assumed that the number of targets, RCS coefficients, Doppler velocities, angular and range bins in which the targets are present are unknown to the radar TRX. The number of probing signal vectors D' in a block is set as $D' = 33$ and the FFT size is $K = D' + R - 1 = 64$. The elements of the probing signal vector $\mathbf{x}(d)$ are drawn from an 8-PSK (phase shift keying) constellation with an average power of unity. The RCS coefficients are randomly initialized from a zero-mean and unit variance circularly symmetric complex Gaussian distribution and the noise is considered to be circularly symmetric complex Gaussian with mean zero and unit variance. A comprehensive list of the various simulation parameters and their values are given in Table 2. The results obtained for various scenarios are elaborated next.

A. STATIONARY TARGETS AND RADAR PLATFORM

For a stationary scenario, $L = 10$ targets were placed at some angle and range bins in the scattering environment by randomly selecting L grid points from the angle-range grid

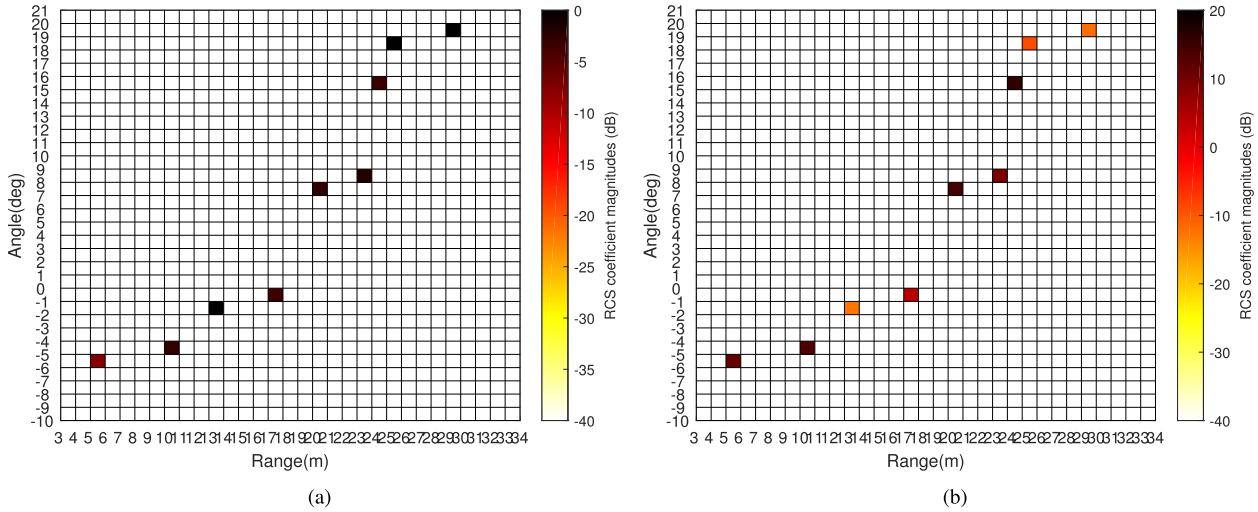

FIGURE 7. Mobile mMR system: (a) True radar image of target RCS values; (b) True Doppler velocity image of scattering scene.

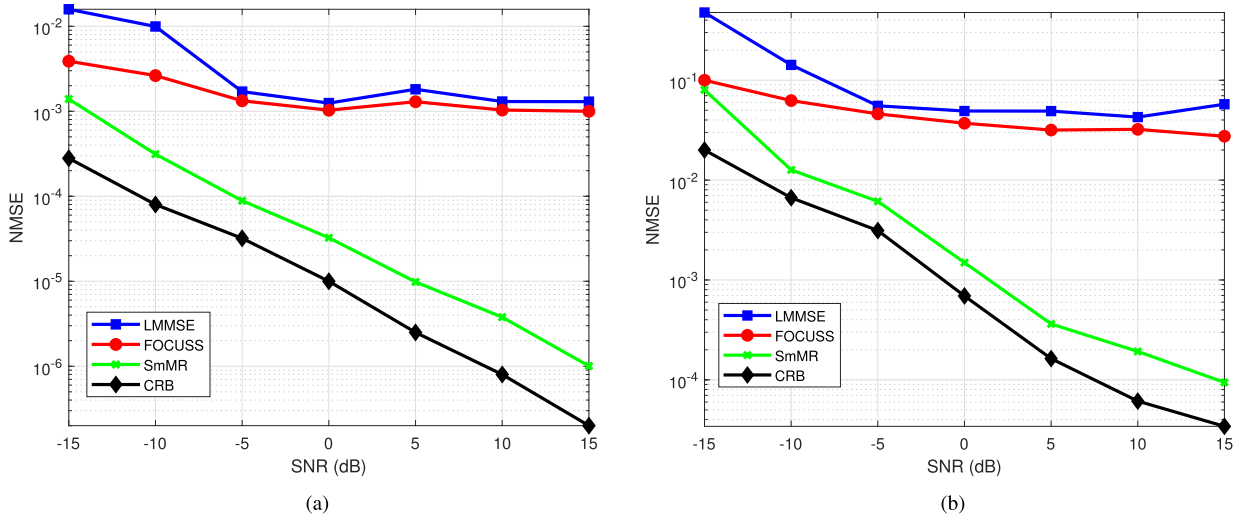

FIGURE 8. For a mobile mMR system: (a) NMSE of RCS estimation vs. SNR for various schemes; (b) NMSE of Doppler velocity estimates vs. SNR for various schemes.

TABLE 2. Simulation parameters.

Symbol	Parameter	Value
N_T	# Transmit antenna	8
N_R	# Receive antenna	16
$N_T^R F$	# Transmit RF chains	4
$N_R^R F$	# Receive RF chains	6
λ	wavelength	0.0107 m
d_T	Transmit antenna spacing	0.7λ
d_R	Receive antenna spacing	0.9λ
L	# targets	10
Q	# angular bins	32
R	# range bins	32
δQ	Angular bin width	1°
δR	Range bin width	1 m
D'	# probing vector	33
K	FFT size	64

of size $Q \times R$. Fig. 4 shows the true radar image obtained by plotting the RCS coefficient matrix against the angle and range bins. The empty bins are indicated by white colors while the colored bins show the RCS coefficient magnitudes in dB, along with the colorbar that maps the intensity of color to dB values given on the right. Fig. 5 shows the normalised MSE (NMSE) performance of the proposed OmMR scheme corresponding to $M = 5$ snapshots. It can be observed that the NMSE of the RCS coefficient vector estimate decreases with increasing signal to noise ratio (SNR), which is along expected lines since probing signals of higher power result in RCS estimates of higher accuracy. Furthermore, it can also be noted that the proposed OmMR scheme performs better than the existing FOCUSS [34] and conventional LMMSE schemes for mMR systems. It may be observed that for a low value of SNR $= -15$ dB, the performance of the OmMR algorithm improves by approximately 20 dB in comparison to the FOCUSS and conventional LMMSE schemes. This is due to the fact that the OmMR efficiently

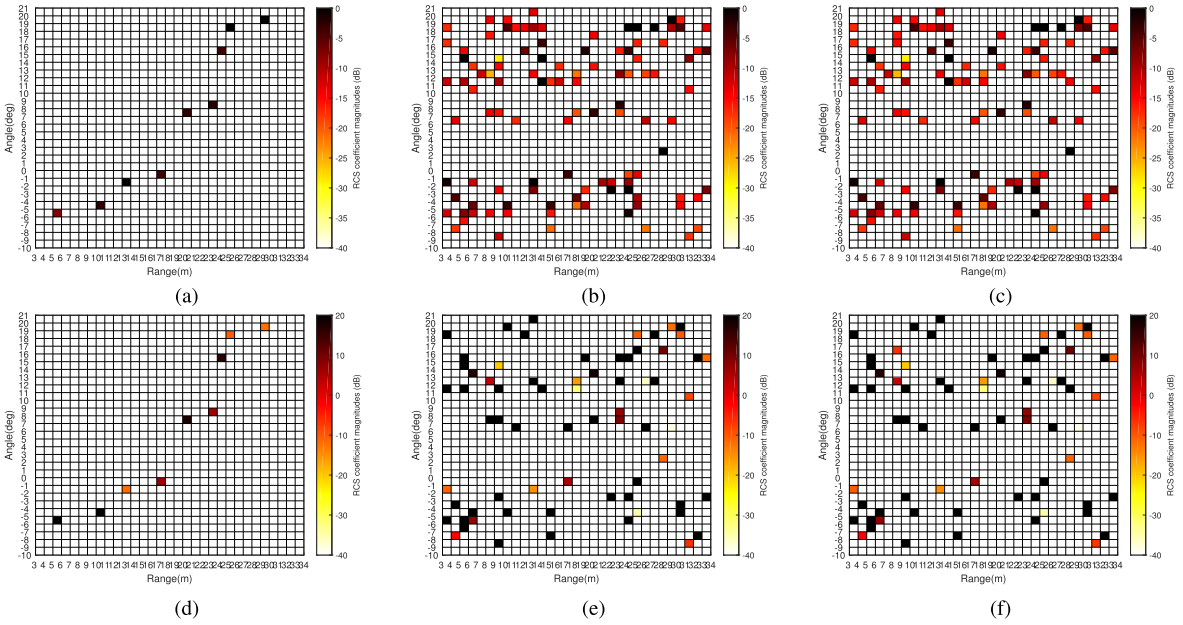

FIGURE 9. For a mobile mMR system: Reconstructed RCS images obtained after thresholding with $\eta_{th} = 0.1$ using (a) proposed SmMR, (b) FOCUSS, (c) LMMSE algorithms at SNR $= -10$ dB; reconstructed Doppler velocity images of the scattering obtained after thresholding with $\eta_{th} = 0.1$ using (d) proposed SmMR, (e) FOCUSS, (f) LMMSE schemes at SNR $= -10$ dB.

exploits the sparsity of the RCS coefficient vector, which leads to a significant improvement in the estimation accuracy. The performance of FOCUSS suffers because it is sensitive to the regularization parameter, which ultimately leads to convergence deficiencies. Note that the LMMSE scheme that does not exploit sparsity has the worst performance. Thus, the performance of FOCUSS and LMMSE schemes is not competitive. On the other hand, the NMSE of the proposed OmMR scheme is seen to be close to the associated CRB derived in Section-V, which demonstrates its efficiency. Remarkably, Fig. 5b shows that the OmMR algorithm for even $M = 5$ snapshots yields an improved performance in comparison to the FOCUSS and the conventional LMMSE schemes with $M = 10, 15$ snapshots. Thus, one can draw a clear conclusion that OmMR can provide accurate estimates even in scenarios with a significantly fewer snapshots of the scattering environment. Fig. 6a-6c show the reconstructed radar images obtained using the OmMR, FOCUSS and conventional LMMSE schemes at SNR $= -10$ dB. One can visually observe that image obtained for OmMR in Fig. 6a is noticeably more accurate when compared to the images obtained using the FOCUSS and conventional LMMSE techniques in Fig. 6b and Fig. 6c, respectively. In fact, one can observe that the reconstructed OmMR image in Fig. 6a accurately maps all the targets to their true angular and range bins shown in Fig. 4. On the other hand, the images obtained using FOCUSS and LMMSE contain several non-zero entries in the estimated RCS coefficient matrix as they fail to efficiently exploit the innate sparsity of the RCS vector and thus are not able to accurately map the targets.

B. MOBILE TARGETS AND RADAR PLATFORM

For the scenario with mobile targets and radar platform, the number of pulses in a block is set as $P = 10$. The vector containing Doppler velocities pertaining to the L targets is set as $\boldsymbol{\upsilon} = [11, 13, -13, 4, 14, 9, 16, -9, -12, 8]^T$. Fig. 7a and Fig. 7b show the true RCS and Doppler images of the radar scattering scene with the side color bars mapping the respective image bin color intensities to dB values of their magnitudes. The threshold η_{th} to determine the non-zero RCS coefficient estimates, and thus obtain an estimate of the total number of targets present in the scattering environment, is set as $\eta_{th} = 0.1$.

Fig. 8a contrasts the NMSE performance of RCS estimation of the proposed SmMR algorithm for the mobile system with that of the FOCUSS and LMMSE techniques along with the associated CRB. As seen for the stationary scenario, the proposed SmMR algorithm results in lower NMSE values as compared to those obtained from the FOCUSS and conventional LMMSE schemes. The poor performance of the LMMSE scheme is attributed to the fact that it fails to exploit the inherent structural sparsity of scattering scene matrix $\mathbf{H}$. Furthermore, the poor performance of FOCUSS is due to its sensitivity to the regularization parameter, which ultimately leads to convergence deficiencies. Fig. 8b plots the NMSE of the Doppler velocity estimates versus SNR. The SmMR is once again seen to result in a significantly improved performance in comparison to the FOCUSS and LMMSE schemes. Furthermore, it can be observed that the minimum NMSE of Doppler velocity estimates that can be achieved using the SmMR is approximately 10^{-4}, which is comparatively higher than NMSE of the RCS

coefficient estimates that is close to 10^{-6} for the same setting. This is due to the fact that estimation of Doppler velocity involves the phase of a ratio which is non-linear in nature. A minute error in estimation of the scattering scene matrix $\mathbf{H}$ can lead to a high NMSE for the Doppler velocity estimates. It is also worth noting that the proposed SmMR scheme achieves an NMSE performance close to the associated CRBs in Fig. 8a and Fig. 8b, which clearly demonstrates its superior estimation and imaging performance. Fig. 9a-9c and Fig. 9d-9f show the reconstructed images for RCS coefficients and relative Doppler velocities at SNR $= -10$ dB. As before, proposed scheme outperforms the FOCUSS and conventional LMMSE schemes, a natural result of the improved NMSE of estimation of the former.

VII. CONCLUSION

This work developed novel parameter estimation and imaging schemes for co-located mMR systems for stationary as well as mobile scenarios. To begin with, the sparse estimation model and an OmMR based RCS coefficient, angle and range estimation algorithm were developed for a scenario with stationary targets and radar platform. Next, the SmMR technique was also developed to estimate the various parameters along with target Doppler velocities considering target and radar mobility. Subsequently, the relevant CRBs were also derived to rigorously characterize the error covariance for estimation of the RCS coefficients and Doppler velocities of multiple targets. Simulation results demonstrated that the proposed techniques yield a significant improvement in performance in comparison to other conventional and competing sparse techniques.

APPENDIX A

The various derivatives of the log likelihood function $\mathcal{L}(\mathbf{y};\Theta)$ with respect to the unknown joint parameter $\Theta = [\bar{\boldsymbol{\gamma}}_{\mathcal{R}}^T, \bar{\boldsymbol{\gamma}}_{\mathcal{I}}^T, \boldsymbol{\upsilon}^T]^T \in \mathbb{R}^{2QR+L\times 1}$ as mentioned in Lemma 1 of section V are derived here. The log likelihood function $\mathcal{L}(\mathbf{y};\Theta)$ is given as

$$\mathcal{L}(\mathbf{y};\Theta) = -\kappa - \sum_{m=0}^{M-1}\sum_{p=0}^{P-1} \|\mathbf{y}(m,p) - \boldsymbol{\Omega}(p)\mathbf{h}(m)\|^2, \quad (47)$$

where $\kappa = \frac{MPKN_{RF}^R}{2}\ln\pi$ and $\mathbf{h}(m) = \text{diag}(\bar{\boldsymbol{\gamma}})\,\mathbf{d}(m) = \text{diag}(\mathbf{d}(m))\,\bar{\boldsymbol{\gamma}}$. The quantity $\frac{\partial\mathcal{L}(\mathbf{y};\Theta)}{\partial\upsilon_l}$ obtained by differentiating the likelihood function with respect to υ_l is given in (39) in section V. Further, one can express the log likelihood function $\mathcal{L}(\mathbf{y};\Theta)$ in terms of the real and imaginary parts of the vector $\mathbf{y}(m,p)$, $\mathbf{h}(m)$ and matrix $\boldsymbol{\Omega}(p)$ as shown in equation (36). Substituting the expression $\mathbf{h}(m)_{\mathcal{R}} = \text{diag}(\mathbf{d}(m))_{\mathcal{R}}\,\bar{\boldsymbol{\gamma}}_{\mathcal{R}} + \text{diag}(\mathbf{d}(m))_{\mathcal{I}}\,\bar{\boldsymbol{\gamma}}_{\mathcal{I}}$ and $\mathbf{h}(m)_{\mathcal{I}} = \text{diag}(\mathbf{d}(m))_{\mathcal{R}}\,\bar{\boldsymbol{\gamma}}_{\mathcal{I}} + \text{diag}(\mathbf{d}(m))_{\mathcal{I}}\,\bar{\boldsymbol{\gamma}}_{\mathcal{R}}$ in the log likelihood function, the intermediate steps to obtain the vector $\frac{\partial\mathcal{L}(\mathbf{y};\Theta)}{\partial\bar{\boldsymbol{\gamma}}_{\mathcal{R}}}$ given in equation (37) are

$$\begin{aligned}\frac{\partial\mathcal{L}(\mathbf{y};\Theta)}{\partial\bar{\boldsymbol{\gamma}}_{\mathcal{R}}} = -\sum_{m=0}^{M-1}\sum_{p=0}^{P-1}\Big(&-2\text{diag}\,(\mathbf{d}(m))_{\mathcal{R}}\,\boldsymbol{\Omega}_{\mathcal{R}}^T(p)\mathbf{y}_{\mathcal{R}}(m,p)\\ &+2\text{diag}\,(\mathbf{d}(m))_{\mathcal{I}}\,\boldsymbol{\Omega}_{\mathcal{I}}^T(p)\mathbf{y}_{\mathcal{R}}(m,p)\\ &-2\text{diag}\,(\mathbf{d}(m))_{\mathcal{R}}\,\boldsymbol{\Omega}_{\mathcal{I}}^T(p)\mathbf{y}_{\mathcal{I}}(m,p)\\ &-2\text{diag}\,(\mathbf{d}(m))_{\mathcal{I}}\,\boldsymbol{\Omega}_{\mathcal{R}}^T(p)\mathbf{y}_{\mathcal{I}}(m,p)\\ &+2\text{diag}\,(\mathbf{d}(m))_{\mathcal{R}}\,\boldsymbol{\Omega}_{\mathcal{R}}^T(p)\boldsymbol{\Omega}_{\mathcal{R}}(p)\text{diag}\,(\mathbf{d}(m))_{\mathcal{R}}\,\bar{\boldsymbol{\gamma}}_{\mathcal{R}}\\ &+2\text{diag}\,(\mathbf{d}(m))_{\mathcal{I}}\,\boldsymbol{\Omega}_{\mathcal{I}}^T(p)\boldsymbol{\Omega}_{\mathcal{I}}(p)\text{diag}\,(\mathbf{d}(m))_{\mathcal{I}}\,\bar{\boldsymbol{\gamma}}_{\mathcal{R}}\Big)\end{aligned} \quad (48)$$

Similarly, $\frac{\partial\mathcal{L}(\mathbf{y};\Theta)}{\partial\bar{\boldsymbol{\gamma}}_{\mathcal{I}}}$ can also be obtained as given in equation (38). The expressions in (41) and (42) can be easily obtained with the help of the first order derivatives $\frac{\partial\mathcal{L}(\mathbf{y};\Theta)}{\partial\bar{\boldsymbol{\gamma}}_{\mathcal{R}}}$, $\frac{\partial\mathcal{L}(\mathbf{y};\Theta)}{\partial\bar{\boldsymbol{\gamma}}_{\mathcal{I}}}$. The intermediate steps to determine the expressions for $\frac{\partial}{\partial\bar{\boldsymbol{\gamma}}_{\mathcal{R}}}\left(\frac{\partial\mathcal{L}(\mathbf{y};\Theta)}{\partial\upsilon_l}\right)$, $\frac{\partial}{\partial\upsilon_l}\left(\frac{\partial\mathcal{L}(\mathbf{y};\Theta)}{\partial\bar{\boldsymbol{\gamma}}_{\mathcal{R}}^T}\right)$ can be found at the top of the page in equations (49) and (50), shown at the top of the next page, respectively.

The expressions in equation (44) can be obtained likewise. Finally, the quantities $\frac{\partial}{\partial\upsilon_{l'}}\left(\frac{\partial\mathcal{L}(\mathbf{y};\Theta)}{\partial\upsilon_l}\right)$, $1 \le l, l' \le L$ are given in equation (51), shown at the top of the next page, where the $\ddot{\mathbf{d}}_l(m) \in \mathbb{C}^{QR\times 1} = \frac{\partial^2\mathbf{d}(m)}{\partial^2\upsilon_l} = [0,\cdots(j\frac{2\pi}{\lambda}mT_m)^2[\mathbf{d}(m)]_{q_l+r_lQ},\cdots,0]^T$. Hence, the Fisher information matrices $\mathcal{F}\left(\bar{\boldsymbol{\gamma}}_{\text{ef}},\bar{\boldsymbol{\gamma}}_{\text{ef}}\right)$, $\mathcal{F}\left(\bar{\boldsymbol{\gamma}}_{\text{ef}},\boldsymbol{\upsilon}\right)$, $\mathcal{F}\left(\boldsymbol{\upsilon},\bar{\boldsymbol{\gamma}}_{\text{ef}}\right)$ and $\mathcal{F}\left(\boldsymbol{\upsilon},\boldsymbol{\upsilon}\right)$ required to compute the CRBs given in equations (30) and (31) are as follows.

1) To begin with, the Fisher information matrices $\mathcal{F}\left(\bar{\boldsymbol{\gamma}}_{\mathcal{R}},\bar{\boldsymbol{\gamma}}_{\mathcal{R}}\right)$, $\mathcal{F}\left(\bar{\boldsymbol{\gamma}}_{\mathcal{I}},\bar{\boldsymbol{\gamma}}_{\mathcal{I}}\right)$, $\mathcal{F}\left(\bar{\boldsymbol{\gamma}}_{\mathcal{R}},\bar{\boldsymbol{\gamma}}_{\mathcal{I}}\right)$ and $\mathcal{F}\left(\bar{\boldsymbol{\gamma}}_{\mathcal{I}},\bar{\boldsymbol{\gamma}}_{\mathcal{R}}\right)$ can be found using equations (41) and (42) given in section V.

$$\begin{aligned}\mathcal{F}\left(\bar{\boldsymbol{\gamma}}_{\mathcal{R}},\bar{\boldsymbol{\gamma}}_{\mathcal{R}}\right) &= \mathcal{F}\left(\bar{\boldsymbol{\gamma}}_{\mathcal{I}},\bar{\boldsymbol{\gamma}}_{\mathcal{I}}\right)\\ &= 2\sum_{m=0}^{M-1}\sum_{p=0}^{P-1}\text{diag}\,(\mathbf{d}(m))\;\boldsymbol{\Sigma}_{\text{c}}\,\text{diag}\,(\mathbf{d}(m))\,,\end{aligned} \quad (52)$$

$$\mathcal{F}\left(\bar{\boldsymbol{\gamma}}_{\mathcal{R}},\bar{\boldsymbol{\gamma}}_{\mathcal{I}}\right) = \mathcal{F}\left(\bar{\boldsymbol{\gamma}}_{\mathcal{I}},\bar{\boldsymbol{\gamma}}_{\mathcal{R}}\right) = \mathbf{0}_{QR,QR}, \quad (53)$$

where $\boldsymbol{\Sigma}_{\text{c}} = \mathbb{E}\{\boldsymbol{\Omega}^T(p)\boldsymbol{\Omega}(p)\}$. Subsequently one can derive the expression for $\mathcal{F}\left(\bar{\boldsymbol{\gamma}}_{\text{ef}},\bar{\boldsymbol{\gamma}}_{\text{ef}}\right)$ given in Lemma 1 of section V.

2) The vectors $\mathcal{F}\left(\bar{\boldsymbol{\gamma}}_{\mathcal{R}},\upsilon_l\right)$, $\mathcal{F}\left(\upsilon_l,\bar{\boldsymbol{\gamma}}_{\mathcal{R}}\right)$ and $\mathcal{F}\left(\bar{\boldsymbol{\gamma}}_{\mathcal{I}},\upsilon_l\right)$, $\mathcal{F}\left(\upsilon_l,\bar{\boldsymbol{\gamma}}_{\mathcal{I}}\right)$ are obtained using the expressions (43) and (44) respectively and are mentioned in Lemma 1 of section V. Therefore, the matrices $\mathcal{F}\left(\bar{\boldsymbol{\gamma}}_{\text{ef}},\boldsymbol{\upsilon}\right)$ and $\mathcal{F}\left(\boldsymbol{\upsilon},\bar{\boldsymbol{\gamma}}_{\text{ef}}\right)$ are obtained as

$$\begin{aligned}\mathcal{F}\left(\bar{\boldsymbol{\gamma}}_{\text{ef}},\boldsymbol{\upsilon}\right) &= \Big[\underbrace{\left[\mathcal{F}\left(\bar{\boldsymbol{\gamma}}_{\mathcal{R}},\upsilon_1\right),\cdots,\mathcal{F}\left(\bar{\boldsymbol{\gamma}}_{\mathcal{R}},\upsilon_L\right)\right]^T}_{\mathcal{F}(\bar{\boldsymbol{\gamma}}_{\mathcal{R}},\boldsymbol{\upsilon})},\\ &\qquad\underbrace{\left[\mathcal{F}\left(\bar{\boldsymbol{\gamma}}_{\mathcal{I}},\upsilon_1\right),\cdots,\mathcal{F}\left(\bar{\boldsymbol{\gamma}}_{\mathcal{I}},\upsilon_L\right)\right]^T}_{\mathcal{F}(\bar{\boldsymbol{\gamma}}_{\mathcal{I}},\boldsymbol{\upsilon})}\Big]\\ &= \mathcal{F}\left(\boldsymbol{\upsilon},\bar{\boldsymbol{\gamma}}_{\text{ef}}\right)^T.\end{aligned} \quad (54)$$

$$\frac{\partial}{\partial \bar{\boldsymbol{\gamma}}_{\mathcal{R}}}\left(\frac{\partial \mathcal{L}(\mathbf{y};\Theta)}{\partial \upsilon_l}\right) = -\sum_{m=0}^{M-1}\sum_{p=0}^{P-1}\Big(-2\left(\text{diag}\left(\dot{\mathbf{d}}_l(m)^*\right)\boldsymbol{\Omega}^H(p)\mathbf{y}(m,p)\right)_{\mathcal{R}} + 2\left(\text{diag}\left(\mathbf{d}(m)^*\right)\boldsymbol{\Omega}^H(p)\boldsymbol{\Omega}(p)\text{diag}\left(\dot{\mathbf{d}}_l(m)\right)\bar{\boldsymbol{\gamma}}\right)_{\mathcal{R}}$$
$$+2\left(\text{diag}\left(\dot{\mathbf{d}}_l(m)^*\right)\boldsymbol{\Omega}^H(p)\boldsymbol{\Omega}(p)\text{diag}\left(\mathbf{d}(m)\right)\bar{\boldsymbol{\gamma}}\right)_{\mathcal{R}}\Big), \tag{49}$$

$$\frac{\partial}{\partial \upsilon_l}\left(\frac{\partial \mathcal{L}(\mathbf{y};\Theta)}{\partial \bar{\boldsymbol{\gamma}}_{\mathcal{R}}^T}\right) = -\sum_{m=0}^{M-1}\sum_{p=0}^{P-1}\Big(-2\left(\mathbf{y}(m,p)^T\boldsymbol{\Omega}(p)\text{diag}\left(\dot{\mathbf{d}}_l(p)\right)\right)_{\mathbf{R}} + 2\left(\bar{\boldsymbol{\gamma}}^T\text{diag}\left(\mathbf{d}(m)\right)\boldsymbol{\Omega}^T(p)\boldsymbol{\Omega}(p)\text{diag}\left(\dot{\mathbf{d}}_l(m)\right)\right)_{\mathcal{R}}$$
$$+2\left(\bar{\boldsymbol{\gamma}}^T\text{diag}\left(\dot{\mathbf{d}}_l(m)\right)\boldsymbol{\Omega}^T(p)\boldsymbol{\Omega}(p)\text{diag}\left(\mathbf{d}(m)\right)\right)_{\mathcal{R}}\Big), \tag{50}$$

$$\begin{aligned}\frac{\partial}{\partial \upsilon_l'}\left(\frac{\partial \mathcal{L}(\mathbf{y};\Theta)}{\partial \upsilon_l}\right) &= -\sum_{m=0}^{M-1}\sum_{p=0}^{P-1}\Big(-2\mathbf{y}^H(m,p)\boldsymbol{\Omega}\text{diag}\left(\bar{\boldsymbol{\gamma}}\right)\ddot{\mathbf{d}}_l(m) + 2\mathbf{d}^H(m)\text{diag}\left(\bar{\boldsymbol{\gamma}}^*\right)\boldsymbol{\Omega}(m)^H\boldsymbol{\Omega}(m)\text{diag}\left(\bar{\boldsymbol{\gamma}}\right)\ddot{\mathbf{d}}_l(m)\\ &\quad +2\dot{\mathbf{d}}_l^H(m)\text{diag}\left(\bar{\boldsymbol{\gamma}}^*\right)\boldsymbol{\Omega}^H(p)\boldsymbol{\Omega}(p)\text{diag}\left(\bar{\boldsymbol{\gamma}}\right)\dot{\mathbf{d}}_l(m)\Big), \text{ for } l = l',\\ &= -\sum_{m=0}^{M-1}\sum_{p=0}^{P-1}\Big(-2\mathbf{v}^H(m,p)\boldsymbol{\Omega}(p)\text{diag}\left(\bar{\boldsymbol{\gamma}}\right)\ddot{\mathbf{d}}_l(m) + 2\dot{\mathbf{d}}_l^H(m)\text{diag}\left(\bar{\boldsymbol{\gamma}}^*\right)\boldsymbol{\Omega}^H(p)\boldsymbol{\Omega}(p)\text{diag}\left(\bar{\boldsymbol{\gamma}}\right)\dot{\mathbf{d}}_l(m)\Big), \text{ for } l = l',\\ &= -\sum_{m=0}^{M-1}\sum_{p=0}^{P-1}\Big(-2\dot{\mathbf{d}}_{l'}^H(m)\text{diag}\left(\bar{\boldsymbol{\gamma}}^*\right)\boldsymbol{\Omega}^H(p)\boldsymbol{\Omega}(p)\text{diag}\left(\bar{\boldsymbol{\gamma}}\right)\dot{\mathbf{d}}_l(m)\Big), \text{ for } l \neq l',\end{aligned} \tag{51}$$

3) Finally, using the result for $\mathcal{F}(\upsilon_{l'}, \upsilon_l)$, $1 \le l, l' \le L$ given in Lemma 1 of section V, one obtains the Fisher information matrix $\mathcal{F}(\boldsymbol{\upsilon}, \boldsymbol{\upsilon})$ invoking the relation

$$\mathcal{F}(\boldsymbol{\upsilon}, \boldsymbol{\upsilon}) = \begin{bmatrix} \mathcal{F}(\upsilon_1, \upsilon_1) & \cdots & \mathcal{F}(\upsilon_1, \upsilon_L) \\ \vdots & & \vdots \\ \mathcal{F}(\upsilon_L, \upsilon_1) & \cdots & \mathcal{F}(\upsilon_L, \upsilon_L) \end{bmatrix}. \tag{55}$$

The CRB for the estimation of the RCS coefficient vector $\bar{\boldsymbol{\gamma}}_{\text{ef}}$ for the stationary mMR system is given as follows. The log likelihood function $\mathcal{L}(\mathbf{y}; \bar{\boldsymbol{\gamma}}_{\text{ef}})$ of the vector received at the output $\mathbf{y} = \left[\mathbf{y}^T(0), \cdots, \mathbf{y}^T(M-1)\right]^T \in \mathbb{C}^{N_{RF}^R KM \times 1}$ with $\mathbf{y}(m)$ defined in equation (16) is given as

$$\begin{aligned}&\mathcal{L}(\mathbf{y}; \bar{\boldsymbol{\gamma}}_{\text{ef}})\\ &= -\kappa\\ &\quad -\sum_{m=0}^{M-1}\sum_{p=0}^{P-1}\|\mathbf{y}_{\mathcal{R}}(m,p) - \boldsymbol{\Omega}_{\mathcal{R}}(p)\bar{\boldsymbol{\gamma}}_{\mathcal{R}}(m) + \boldsymbol{\Omega}_{\mathcal{I}}(p)\bar{\boldsymbol{\gamma}}_{\mathcal{I}}(m)\|^2\\ &\quad -\sum_{m=0}^{M-1}\sum_{p=0}^{P-1}\|\mathbf{y}_{\mathcal{I}}(m,p) - \boldsymbol{\Omega}_{\mathcal{I}}(p)\bar{\boldsymbol{\gamma}}_{\mathcal{R}}(m) - \boldsymbol{\Omega}_{\mathcal{R}}(p)\bar{\boldsymbol{\gamma}}_{\mathcal{I}}(m)\|^2,\end{aligned} \tag{56}$$

where $\kappa = \frac{MKN_{RF}^R}{2}\ln\pi$. The individual components of the Fisher information matrix $\mathcal{F}\left(\bar{\boldsymbol{\gamma}}_{\text{ef}}\right) \in \mathbb{R}^{2QR\times 2QR}$ are given as

$$\begin{aligned}\mathcal{F}\left(\bar{\boldsymbol{\gamma}}_{\mathcal{R}}, \bar{\boldsymbol{\gamma}}_{\mathcal{R}}\right) &= -\mathbb{E}\left\{\frac{\partial}{\partial \bar{\boldsymbol{\gamma}}_{\mathcal{R}}}\frac{\partial}{\partial \bar{\boldsymbol{\gamma}}_{\mathcal{R}}}^T\mathcal{L}(\mathbf{y};\bar{\boldsymbol{\gamma}})\right\}\\ &= 2\sum_{m=0}^{M-1}\mathbb{E}\left\{\boldsymbol{\Omega}^T(m)\boldsymbol{\Omega}(m)\right\} = 2M\boldsymbol{\Sigma}_{\text{c}},\\ \mathcal{F}\left(\bar{\boldsymbol{\gamma}}_{\mathcal{I}}, \bar{\boldsymbol{\gamma}}_{\mathcal{I}}\right) &= -\mathbb{E}\left\{\frac{\partial}{\partial \bar{\boldsymbol{\gamma}}_{\mathcal{I}}}\frac{\partial}{\partial \bar{\boldsymbol{\gamma}}_{\mathcal{I}}}^T\mathcal{L}(\mathbf{y};\bar{\boldsymbol{\gamma}})\right\}\\ &= 2\sum_{m=0}^{M-1}\mathbb{E}\left\{\boldsymbol{\Omega}^T(m)\boldsymbol{\Omega}(m)\right\} = 2M\boldsymbol{\Sigma}_{\text{c}},\\ \mathcal{F}\left(\bar{\boldsymbol{\gamma}}_{\mathcal{R}}, \bar{\boldsymbol{\gamma}}_{\mathcal{I}}\right) &= -\mathbb{E}\left\{\frac{\partial}{\partial \bar{\boldsymbol{\gamma}}_{\mathcal{R}}}\frac{\partial}{\partial \bar{\boldsymbol{\gamma}}_{\mathcal{I}}}^T\mathcal{L}(\mathbf{y};\bar{\boldsymbol{\gamma}})\right\} = \mathbf{0}_{QR,QR},\\ \mathcal{F}\left(\bar{\boldsymbol{\gamma}}_{\mathcal{I}}, \bar{\boldsymbol{\gamma}}_{\mathcal{R}}\right) &= -\mathbb{E}\left\{\frac{\partial}{\partial \bar{\boldsymbol{\gamma}}_{\mathcal{I}}}\frac{\partial}{\partial \bar{\boldsymbol{\gamma}}_{\mathcal{R}}}^T\mathcal{L}(\mathbf{y};\bar{\boldsymbol{\gamma}})\right\} = \mathbf{0}_{QR,QR}.\end{aligned}$$

Using these results, one can readily obtain $\text{CRB}(\bar{\boldsymbol{\gamma}}_{\text{ef}})$ as

$$\text{CRB}\left(\bar{\boldsymbol{\gamma}}_{\text{ef}}\right) = \frac{1}{2M}\left(\mathbf{I}_2 \otimes \boldsymbol{\Sigma}_{\text{c}}^{-1}\right). \tag{57}$$

REFERENCES

[1] X. Li, X. Wang, Q. Yang, and S. Fu, "Signal processing for TDM MIMO FMCW millimeter-wave radar sensors," *IEEE Access*, vol. 9, pp. 167959–167971, 2021.

[2] C. Vasanelli, R. Batra, A. D. Serio, F. Boegelsack, and C. Waldschmidt, "Assessment of a millimeter-wave antenna system for MIMO radar applications," *IEEE Antennas Wireless Propag. Lett.*, vol. 16, pp. 1261–1264, 2017.

[3] K. Sakaguchi, R. Fukatsu, T. Yu, E. Fukuda, K. Mahler, R. Heath, T. Fujii, K. Takahashi, A. Khoryaev, S. Nagata, and T. Shimizu, "Towards mmWave V2X in 5G and beyond to support automated driving," 2020, *arXiv:2011.09590*.

[4] F. Liu and C. Masouros, "A tutorial on joint radar and communication transmission for vehicular networks—Part I: Background and fundamentals," *IEEE Commun. Lett.*, vol. 25, no. 2, pp. 322–326, Feb. 2021.

[5] K. V. Mishra, M. R. B. Shankar, V. Koivunen, B. Ottersten, and S. A. Vorobyov, "Toward millimeter-wave joint radar communications: A signal processing perspective," *IEEE Signal Process. Mag.*, vol. 36, no. 5, pp. 100–114, Sep. 2019.

[6] K. V. Mishra and Y. C. Eldar, "Sub-Nyquist channel estimation over IEEE 802.11ad link," in *Proc. Int. Conf. Sampling Theory Appl. (SampTA)*, Jul. 2017, pp. 355–359.

[7] J. Hatch, A. Topak, R. Schnabel, T. Zwick, R. Weigel, and C. Waldschmidt, "Millimeter-wave technology for automotive radar sensors in the 77 GHz frequency band," *IEEE Trans. Microw. Theory Techn.*, vol. 60, no. 3, pp. 845–860, Mar. 2012.

[8] M. Lesturgie, "T06—MIMO radar," in *Proc. IEEE Radar Conf.*, May 2014, p. 33.

[9] J. Li and P. Stoica, "MIMO radar with colocated antennas," *IEEE Signal Process. Mag.*, vol. 24, no. 5, pp. 106–114, Sep. 2007.

[10] J. L. P. Stoica, *MIMO Radar Signal Processing*. Hoboken, NJ, USA: Wiley, 2009.

[11] D. W. Bliss and K. W. Forsythe, "Multiple-input multiple-output (MIMO) radar and imaging: Degrees of freedom and resolution," in *Proc. IEEE Conf. Rec. 37th Asilomar Conf. Signals, Syst. Comput.*, vol. 1, Nov. 2003, pp. 54–59.

[12] E. Fishler, A. Haimovich, R. Blum, L. Cimini, D. Chizhik, and R. Valenzuela, "Spatial diversity in radars—Models and detection performance," *IEEE Trans. Signal Process.*, vol. 54, no. 3, pp. 823–838, Mar. 2006.

[13] I. Bekkerman and J. Tabrikian, "Target detection and localization using MIMO radars and sonars," *IEEE Trans. Signal Process.*, vol. 54, no. 10, pp. 3873–3883, Oct. 2006.

[14] L. Xu and J. Li, "Iterative generalized-likelihood ratio test for MIMO radar," *IEEE Trans. Signal Process.*, vol. 55, no. 6, pp. 2375–2385, Jun. 2007.

[15] S. Li, L. Zhang, N. Liu, J. Zhang, and S. Zhao, "Range-angle dependent detection for FDA-MIMO radar," in *Proc. CIE Int. Conf. Radar (RADAR)*, Oct. 2016, pp. 1–4.

[16] X. Zhang and D. Xu, "Low-complexity ESPRIT-based DOA estimation for colocated MIMO radar using reduced-dimension transformation," *Electron. Lett.*, vol. 47, no. 4, pp. 283–284, 2011.

[17] M. Yang, B. Chen, G. Zheng, and X. Dang, "Reduced-dimensional ESPRIT algorithm for MIMO radar," in *Proc. IEEE CIE Int. Conf. Radar*, Oct. 2011, pp. 347–349.

[18] N. Liu, L. R. Zhang, J. Zhang, and D. Shen, "Direction finding of MIMO radar through ESPRIT and Kalman filter," *Electron. Lett.*, vol. 45, no. 17, pp. 908–910, Aug. 2009.

[19] J. Capon, "High-resolution frequency-wavenumber spectrum analysis," *Proc. IEEE*, vol. 57, no. 8, pp. 1408–1418, Aug. 1969.

[20] E. G. Larsson, J. Li, and P. Stoica, "High-resolution nonparametric spectral analysis: Theory and applications," in *High-Resolution Robust Signal Processing*. Boca Raton, FL, USA: CRC Press, 2017, pp. 151–252.

[21] A. Jakobsson and P. Stoica, "Combining Capon and APES for estimation of spectral lines," *Circuits, Syst., Signal Process.*, vol. 19, no. 2, pp. 159–169, Mar. 2000.

[22] X. Zhang and D. Xu, "Angle estimation in MIMO radar using reduced-dimension Capon," *Electron. Lett.*, vol. 46, no. 12, pp. 860–861, Jun. 2010.

[23] L. Xu, J. Li, and P. Stoica, "Target detection and parameter estimation for MIMO radar systems," *IEEE Trans. Aerosp. Electron. Syst.*, vol. 44, no. 3, pp. 927–939, Jul. 2008.

[24] T. Yardibi, J. Li, and P. Stoica, "Nonparametric and sparse signal representations in array processing via iterative adaptive approaches," in *Proc. 42nd Asilomar Conf. Signals, Syst. Comput.*, Oct. 2008, pp. 278–282.

[25] W. Roberts, P. Stoica, J. Li, T. Yardibi, and F. A. Sadjadi, "Iterative adaptive approaches to MIMO radar imaging," *IEEE J. Sel. Topics Signal Process.*, vol. 4, no. 1, pp. 5–20, Feb. 2010.

[26] A. Rawat, S. Dwivedi, and A. K. Jagannatham, "BLMS and FBLMS-based adaptive time varying RCS estimation and 2D-imaging for monostatic MIMO radar systems," in *Proc. 23rd Nat. Conf. Commun. (NCC)*, Mar. 2017, pp. 1–6.

[27] S. Dwivedi, P. Aggarwal, and A. K. Jagannatham, "Fast block LMS and RLS-based parameter estimation and two-dimensional imaging in monostatic MIMO RADAR systems with multiple mobile targets," *IEEE Trans. Signal Process.*, vol. 66, no. 7, pp. 1775–1790, Apr. 2018.

[28] A. Rawat, S. Dwivedi, S. Srivastava, and A. K. Jagannatham, "RLS-based adaptive time-varying RCS estimation and imaging in MIMO radar systems," in *Proc. Nat. Conf. Commun. (NCC)*, Feb. 2020, pp. 1–6.

[29] Y. C. Lin, T. S. Lee, Y. H. Pan, and K. H. Lin, "Low-complexity high-resolution parameter estimation for automotive MIMO radars," *IEEE Access*, vol. 8, pp. 16127–16138, 2020.

[30] A. B. Baral and M. Torlak, "Joint Doppler frequency and direction of arrival estimation for TDM MIMO automotive radars," *IEEE J. Sel. Topics Signal Process.*, vol. 15, no. 4, pp. 980–995, Jun. 2021.

[31] S. Lim, J. Jung, J. Kim, S.-C. Kim, and J. Choi, "Enhanced velocity estimation based on joint Doppler frequency and range rate measurements," in *Proc. 13th Int. Conf. Ubiquitous Future Netw. (ICUFN)*, Jul. 2022, pp. 217–221.

[32] C. Wen, Y. Xie, Z. Qiao, L. Xu, and Y. Qian, "A tensor generalized weighted linear predictor for FDA-MIMO radar parameter estimation," *IEEE Trans. Veh. Technol.*, vol. 71, no. 6, pp. 6059–6072, Jun. 2022.

[33] R. Tibshirani, "Regression shrinkage and selection via the lasso," *J. Roy. Statist. Soc., B, Methodolog.*, vol. 58, no. 1, pp. 267–288, 1996.

[34] I. F. Gorodnitsky and B. D. Rao, "Sparse signal reconstruction from limited data using FOCUSS: A re-weighted minimum norm algorithm," *IEEE Trans. Signal Process.*, vol. 45, no. 3, pp. 600–616, Mar. 1997.

[35] P. Chen, Z. Cao, Z. Chen, and X. Wang, "Off-grid DOA estimation using sparse Bayesian learning in MIMO radar with unknown mutual coupling," *IEEE Trans. Signal Process.*, vol. 67, no. 1, pp. 208–220, Jan. 2019.

[36] T. Liu, F. Wen, L. Zhang, and K. Wang, "Off-grid DOA estimation for colocated MIMO radar via reduced-complexity sparse Bayesian learning," *IEEE Access*, vol. 7, pp. 99907–99916, 2019.

[37] X. Zhao, C. Guo, and W. Peng, "Joint estimation of multiple parameters in bistatic MIMO radar based on sparse signal restoration," in *Proc. Int. Conf. Microw. Millim. Wave Technol. (ICMMT)*, May 2018, pp. 1–3.

[38] C.-Y. Wu, T. Zhang, J. Li, and T. F. Wong, "Parameter estimation in PMCW MIMO radar systems with few-bit quantized observations," *IEEE Trans. Signal Process.*, vol. 70, pp. 810–821, 2022.

[39] Z. Chen, W. Ma, P. Chen, and Z. Cao, "A robust sparse Bayesian learning-based DOA estimation method with phase calibration," *IEEE Access*, vol. 8, pp. 141511–141522, 2020.

[40] R. W. Heath, N. González-Prelcic, S. Rangan, W. Roh, and A. M. Sayeed, "An overview of signal processing techniques for millimeter wave MIMO systems," *IEEE J. Sel. Topics Signal Process.*, vol. 10, no. 3, pp. 436–453, Feb. 2016.

[41] F. Sohrabi and W. Yu, "Hybrid digital and analog beamforming design for large-scale antenna arrays," *IEEE J. Sel. Topics Signal Process.*, vol. 10, no. 3, pp. 501–513, Apr. 2016.

[42] O. El Ayach, S. Rajagopal, S. Abu-Surra, Z. Pi, and R. W. Heath, Jr., "Spatially sparse precoding in millimeter wave MIMO systems," *IEEE Trans. Wireless Commun.*, vol. 13, no. 3, pp. 1499–1513, Jan. 2014.

[43] A. Alkhateeb, G. Leus, and R. W. Heath, "Limited feedback hybrid precoding for multi-user millimeter wave systems," *IEEE Trans. Wireless Commun.*, vol. 14, no. 11, pp. 6481–6494, Nov. 2015.

[44] S. M. Kay, *Fundamentals of Statistical Signal Processing: Estimation Theory*. Upper Saddle River, NJ, USA: Prentice-Hall, 1993.

[45] K. Venugopal, A. Alkhateeb, N. González-Prelcic, and R. W. Heath, Jr., "Channel estimation for hybrid architecture-based wideband millimeter wave systems," *IEEE J. Sel. Areas Commun.*, vol. 35, no. 9, pp. 1996–2009, Sep. 2017.

[46] D. P. Wipf and B. D. Rao, "Sparse Bayesian learning for basis selection," *IEEE Trans. Signal Process.*, vol. 52, no. 8, pp. 2153–2164, Aug. 2004.

[47] M. Rossi, A. M. Haimovich, and Y. C. Eldar, "Spatial compressive sensing in MIMO radar with random arrays," in *Proc. 46th Annu. Conf. Inf. Sci. Syst. (CISS)*, Mar. 2012, pp. 1–6.

MEESAM JAFRI (Student Member, IEEE) received the B.E. degree in electronics and communication engineering from Jamia Millia Islamia, New Delhi, India, in 2016, and the M.Tech. degree in communication and information technology from the National Institute of Technology Srinagar, India, in 2018. He is currently pursuing the Ph.D. degree with the Department of Electrical Engineering, Indian Institute of Technology Kanpur, Kanpur, India. His research interests include coordinated beamforming in 5G wireless systems, mmWave communication, orthogonal time-frequency space (OTFS), radar signal processing, and joint radar and communication (RadCom). He was awarded Qualcomm Innovation Fellowship (QIF) from Qualcomm, in 2022.

SURAJ SRIVASTAVA (Member, IEEE) received the M.Tech. degree in electronics and communication engineering from the Indian Institute of Technology Roorkee, India, in 2012, and the Ph.D. degree in electrical engineering from the Indian Institute of Technology Kanpur, Kanpur, India, in 2022. From July 2012 to November 2013, he was employed as a Staff-I Systems Design Engineer with Broadcom Research India Pvt. Ltd., Bengaluru, and from November 2013 to December 2015, he was employed as a Lead Engineer with Samsung Research India, Bengaluru, where he worked on developing layer-2 of the 3G UMTS/WCDMA/HSDPA modem. His research interests include applications of sparse signal processing in 5G wireless systems, mmWave and terahertz communication, orthogonal time-frequency space (OTFS), joint radar and communication (RadCom), and optimization and machine learning. He was awarded the Outstanding Ph.D. Thesis and Outstanding Teaching Assistant Awards from the IIT Kanpur. He was awarded Qualcomm Innovation Fellowship (QIF) from Qualcomm, in 2018 and 2022.

SANA ANWER received the B.Tech. degree in electronics and communication engineering from the J. K. Institute of Applied Physics and Technology, University of Allahabad, Prayagraj, India, in 2019, and the M.Tech. degree in electrical engineering with specialization in signal processing, communication and networking from the Indian Institute of Technology Kanpur, Kanpur, India, in 2022. She is currently a Systems Engineer with Qualcomm, Hyderabad, India. Her research interests include joint sensing and communication systems, radar signal processing, orthogonal time-frequency space (OTFS), and mmWave communications.

ADITYA K. JAGANNATHAM (Senior Member, IEEE) received the bachelor's degree from the Indian Institute of Technology, Bombay, and the M.S. and Ph.D. degrees from the University of California at San Diego, San Diego, CA, USA. From April 2007 to May 2009, he was employed as a Senior Wireless Systems Engineer with Qualcomm Inc., San Diego, where he was a part of the Qualcomm CDMA Technologies (QCT) Division. He is currently a Professor with the Department of Electrical Engineering, IIT Kanpur, where he also holds the Arun Kumar Chair Professorship. His research interests include next-generation wireless cellular and WiFi networks, with a special emphasis on various 5G technologies, and such as massive MIMO, mmWave MIMO, FBMC, NOMA, and full duplex. He has been twice awarded the P. K. Kelkar Young Faculty Research Fellowship for excellence in research, the Qualcomm Innovation Fellowship (QInF), the IIT Kanpur Excellence in Teaching Award, the CAL(IT)2 Fellowship at the University of California at San Diego, and the Upendra Patel Achievement Award at Qualcomm.